Politecnico di Torino

Politecnico di Torino

Corso di Laurea in Ingegneria Biomedica
A.a. 2020/2021
Sessione di Laurea dicembre 2021

Effects of electromagnetic fields on microtubule dynamics

Relatore:
Jacek Adam Tuszynski

Candidato:
Elisabetta Di Gregorio

Index

1. Abstract

Cancer is one of the leading causes of death around the globe. Existing drugs and treatments have made substantial progress and improved patients' life expectancy; nevertheless, it is impossible to overlook that they yield serious adverse effects. A novel strategy is required to overcome these flaws, and electromagnetic fields have appeared to be a promising candidate. In recent years, their exploitation has taken hold more and more, with the benefits of fewer side effects, higher efficiency, a wide range of uses at lower costs. Here we investigate the application of two kinds of electromagnetic fields: terahertz radiation and near-infrared excitation. In particular, we examined the effect that these types of emissions have on microtubules, critical cytoskeletal structures that regulate a wide range of biological functions as cell division, shaping, motility, and intracellular transport. Selective stabilization of microtubules that come into contact with chromosomes during mitosis is hypothesized to aid in the formation of the mitotic spindle, which is pivotal in cell division. Proliferation is one of the characteristic hallmarks of cancer cells which makes this disease so difficult to control. Acting on microtubule dynamics could be the key to preventing cancer cells from spreading uncontrollably. We used Raman spectroscopy analysis and turbidity measurements as effective methodologies to keep track of tubulin changes after the exposition, enabling us to witness the effect of electromagnetic fields on microtubule dynamics.

2. Introduction

2.1. *The importance of microtubules*

Microtubules (MTs) are hollow fibres that are found in all eukaryotic cells as part of the cytoskeleton or spindle figure. Their role is essential in cell division, shaping, motility, and intracellular transport [1], [2]. The mitotic spindle is a complex and dynamic structure that mediates chromosome separation during mitosis. Indeed, cells that lack a functioning spindle are unable to divide properly and are prone to apoptosis [3].

Despite their functional diversity, MTs have a highly conserved structure composed of heterodimers of globular α-tubulin and β-tubulin molecules; each of which has a molecular weight of 50 kDa. Both subunits have a large amount of sequence homology [1], [2]. In general, tubulin family members are differentiated by sequences at the C-terminal tail that serves as a binding domain for microtubule-associated proteins (MAPs) [4].

MTs are polar structures with two different ends due to the asymmetry of the αβ-tubulin heterodimer. These ends have differing rates of polymerisation: a slow-growing minus (-) end with an exposure α-tubulin subunit and a fast-growing plus (+) end with the β-tubulin subunit.

The two stages of MT assembly are nucleation, which is aided by a third tubulin isoform, γ-tubulin, and elongation, during which αβ-tubulin heterodimers are added to the + end [5]. Indeed, MTs are generated as a result of the 'reversible' polymerization of tubulin, which is a guanine nucleotide-binding protein with one exchangeable and one non-exchangeable binding site. Guanosine-triphosphate (GTP) is required for optimum assembly at both sites. GTP at the exchangeable site is hydrolysed in Guanosine-diphosphate (GDP) and one inorganic phosphate P. This process allows MTs assembly, resulting in a MT that is mostly GDP-tubulin, with a tiny section of GTP-bound tubulin, known as a "GTP cap," at the end. This cap enables the MTs polymerization. Indeed, the loss of the cap causes a transition from growth to shortening (referred to as a "catastrophe"), whereas the reacquisition of the GTP cap causes a transition from shortening to growing (referred to as a "rescue") (Figure 1) [2], [5]. Therefore, MTs are intrinsically dynamic as, by this mechanism called dynamic instability, they can alternate between polymerization phases and spontaneous depolymerization, allowing them to be rapidly reshaped in cells [2], [5].

Temperature is another important factor for tubulin polymerisation. Low temperature prevents MT assembly without reducing tubulin protein levels in the cell. Indeed, temperature-induced depolymerization and polymerization cycles have been utilised to selectively disrupt MT networks in cells and extract tubulin from cells [6].

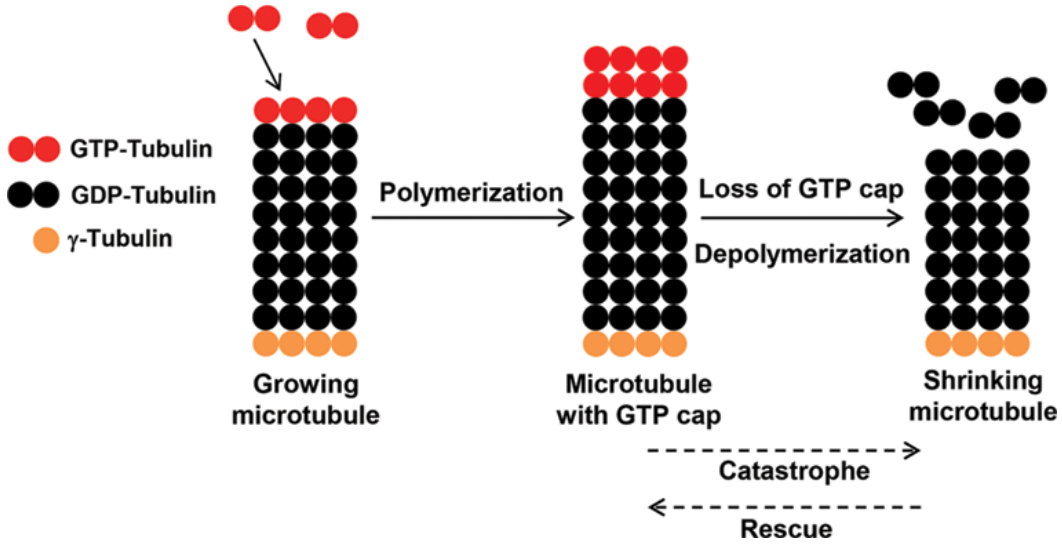

Figure 1. *Microtubule dynamics: Catastrophe and Rescue transitions. This image is displayed with the permission of ref.* [5]

MT dynamics are finely controlled in normal cells, both spatially and temporally, and even across various sections of a cell's cytoplasm. Differential regulation is required for various cellular processes, e.g. MT dynamics substantially increase during mitosis and they are regulated by a variety of endogenous cellular proteins [7].

In particular, MT disassembly results in the formation of mitotic spindles, whereas depolymerization of spindle microtubules, as they reassemble into cytoplasmic microtubules, marks the end of mitosis. If this cycle is interrupted, the cell will either not enter mitosis, or cell division will be hindered, resulting in mitotic arrest or division errors, decreased proliferation, and cell death [4].

This also applies to tumour cells; their division and growth are inhibited when the dynamic behaviour of microtubules is impaired. Therefore, because of their critical role in mitotic cell division, microtubules have become one of the most important targets in many anticancer treatments. Indeed, many anti-angiogenic agents in clinical trials are microtubules targeting agents (MTAs) [4].

2.2. *Microtubules targeting agents (MTAs)*

MTAs, also known as tubulin-binding agents (TBAs), microtubule-interfering or anti-microtubule drugs, or microtubule poisons, are a class of chemical compounds that bind to MTs and change their properties [8]. Indeed, several MTAs bind to β-tubulin and affect MTs function during mitosis, resulting in mitotic arrest and cell death [7]. MTAs are a key anticancer drug family with antimitotic and antiangiogenic characteristics. Their function is to slow tumour growth by affecting MT dynamics in cancer and endothelial cells [8], [9].

Usually, mitotic spindle microtubules attach to the kinetochores of separating chromosomes, ensuring that genetic material is distributed evenly to daughter cells [10]. When chromosomes are not correctly attached or separated, the cell cycle is stopped in the mitotic checkpoint, which results in apoptosis [4].

MTs also play an important role in interphase cells. One well-known role is in vesicular trafficking, where MTs act as platforms for molecular motors. MTAs target all these properties [10], [11].

MTAs can be categorised into two groups: Microtubule-stabilizing agents (MSAs), such as taxanes, epothilones, zampanolide, and laulimalide, and microtubule-destabilizing agents (MDAs), including colchicine, vinca alkaloids, and maytansine [12].

MSAs strengthen the lateral interactions between tubulin heterodimers after binding it, causing greater polymerization and stabilisation of MTs at high compound concentrations, resulting in higher polymer mass within the cell [8]. Many of these drugs (such as epothilone and zampanolide) are classified as taxane-site binders because they target the Taxol binding pocket on the MT lumen [13]. We are choosing to focus primarily on Taxol.

At high doses, MDAs reduce or prevent mostly longitudinal interactions between heterodimers, resulting in MT depolymerization and reduced polymer mass [8]. Colchicine derivates belong to this second category. Even though colchicine is also being studied as a cancer treatment, it was initially approved by the FDA in 2009 as a monotherapy treatment for familial Mediterranean fever and acute gout flares. Colchicine's therapeutic effectiveness against cancer is limited by its low therapeutic index and its side effects [11].

Both forms of MTAs only fine-tune MT dynamics at the lower concentrations utilised in clinical applications, therefore they play little influence on polymer mass or overall cytoskeleton characteristics [8], [14]. The two main issues with MTAs-based cancer therapy are high systemic toxicity and resistance development. MTAs' toxic side effects can be reduced, at least in part, by conjugating the drugs with different carriers [10], [14]. To date, six binding sites on the tubulin surface have been identified (Figure 2), as well as countless small molecules that attach to these pockets and affect intra- and inter tubulin interactions [8]. The ones of our interest are the taxane and the colchicine sites.

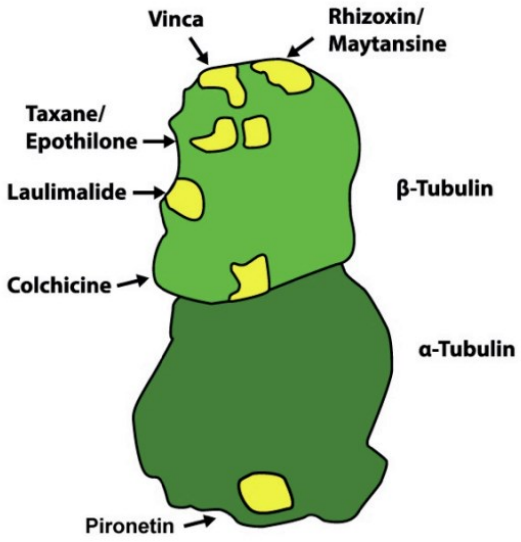

Figure 2. *Representation of the six different tubulin binding sites. This image is displayed with the permission of ref.* [12]

2.2.1. Taxane site

Paclitaxel (Figure 3), whose structure was determined in 1998 based on electron crystallography data acquired from tubulin–paclitaxel zinc sheets, was the first atomic-

level description of an MTA's binding to tubulin [14]. The drug's non-brand name is Paclitaxel, but it is also referred to by one of its brand names, Taxol™. The Food and Drug Administration (FDA) has approved Taxol as an anticancer medication for the treatment of different cancers, including ovarian, breast, and non-small-cell lung carcinomas. It was the first natural product described to stabilise microtubules, and it was isolated from the bark of the Pacific yew, Taxus brevifolia [15].

Its mode of action is still not completely understood but some hypotheses were formulated. Understanding how Taxol and other small molecules alter MT structure will not only help us better understand MT dynamic instability but will also allow us to optimize MSA design in the fight against cancer. According to one of the models, Taxol blocks the structural change that happens when GTP is hydrolysed, at least in part, therefore impairing MTs disassembly [13].

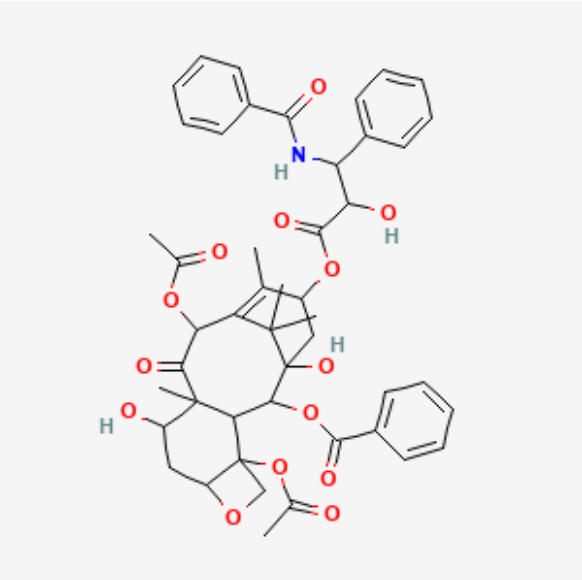

Figure 3. *Taxol chemical structure. PubChem CID 4666. This image is displayed with the permission of ref.* [16]

2.2.2. Colchicine sites

MTAs ligands that bind to the colchicine site are perhaps the most well-studied. The colchicine site is a deep pocket found near the intra-dimer interface between the α- and β-tubulin subunits in the intermediate domain of β-tubulin (Figure 2). The site is organised into two zones: a primary zone in the domain's centre, and two supplementary pockets that face the α-tubulin subunit or are buried deeper in the β-tubulin subunit. All colchicine site's core secondary structural components interact with the ligand in the bound state, mostly through hydrophobic and very few polar interactions [14]. When colchicine and β-tubulin bond, a bent tubulin dimer is created, which prevents it from adopting a straight form and hence inhibits microtubule assembly [11].

In this work, we are going to use CCI-001 (Figure 4), a new tubulin polymerization inhibitor that binds to the colchicine pocket. It was synthesised and patented at the University of Alberta's Department of Oncology (Edmonton, Canada), and has demonstrated potent anti-cancer activity in various cancer cell lines in vitro. Furthermore,

CCI-001 is particularly effective in cancer cells that have demonstrated resistance to paclitaxel [17].

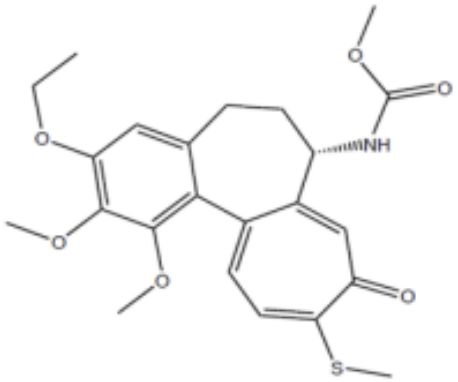

Figure 4. *CCI-001 chemical structure. This image is displayed with the permission of ref.* [17]

Since inhibiting microtubule dynamics is a mechanism used by anti-cancer drugs, disruption of microtubule networks through intense Terahertz (THz) pulses could represent a new possible therapeutic mechanism [18].

2.3. *Terahertz excitation*

THz frequencies are strongly coupled to the natural oscillations of hydrogen bonds found in all proteins and DNA. This interaction provides a unique sensitivity to molecular structure and can alter gene expression and protein structure/function non-thermally [19].

THz radiation is thought to elicit conformational changes in proteins and nucleic acids, which may alter the functional properties of these critical biological components [20]. It should be mentioned that THz radiation should not be regarded as a heat rendering effect, as their quantum energy is insufficient to hydrolyse hydrogen bonds in proteins and other biological macromolecules [21].

Indeed, THz excitation, according to Lundholm et al., promotes non-thermal structural changes associated with Fröhlich condensation in a protein crystal. They discovered that electromagnetic radiation at 0.4 THz causes non-thermal changes in electron density. They found a local rise in electron density in a long alpha (α) helix motif, which is compatible with a minor longitudinal compression of the helix [22]. Terahertz wave radiation does not cause the rupture or rebuilding of chemical covalent bonds; however, it may stimulate the rotational energy level of proteins, causing them to change their spatial conformation and perhaps influencing protein interactions [23]. They may produce intermolecular conformational changes because THz frequency corresponds to intermolecular motions such as vibration, liberation, and rotational relaxation [24], [25].

The following paragraphs will summarise some of the literature available on THz protein exposure.

2.3.1.1. Albumin

Albumin is a globular protein that serves as the primary transport protein in both human and animal blood serum. It is capable of reversible binding and transporting a variety of substances such as hormones, metal ions, fatty acids, and so on. It has been observed that the albumin globule is quite labile and sensitive to even minor actions, making this protein a suitable target for THz exposure [20].

In 1991, Govorun et al. reported that exposing albumin to THz radiation (3.3 THz) resulted in changes in the α-helices content: α-helices content decreases in albumin simultaneously with the changes of the binding capability of this protein. They showed that albumin secondary structure changes linearly according to the dose of laser emission [21].

A later 2009 study confirmed that terahertz irradiation (3.6 THz) induced some dose-dependent changes in albumin. These variations were indicative of conformational changes in the protein molecule and the modification of its functional characteristics [20].

2.3.1.2. Actin

Actin is a highly abundant protein present in eukaryotic cells. It is very conserved and is involved in more protein-protein interactions than any other protein. These characteristics, as well as its ability to transition between monomeric (G-actin) and filamentous (F-actin) states under the control of nucleotide hydrolysis, ions, and many actin-binding proteins, make actin a key player in a wide range of cellular functions, from cell motility to cell shape and polarity maintenance to transcription regulation [26]. Similar to tubulin, actin polymerisation success depends on temperature [27].

In 2018, Yamazaki et al. discovered that THz irradiation at lower peak powers (5.7 mJ/cm^2) activates the elongation phase of the actin polymerization reaction without thermal or acoustic effects or denaturation of its molecular structures [24], [25].

In 2020, Yamazaki et al. offered another take on actin interaction with THz waves. This time, they focused on the indirect effects of THz irradiation. THz pulses cause shockwaves to form on the surface of liquid water. These shockwaves travel many millimetres in depth. THz-induced shockwaves may cause mechanical stress in biomolecules, altering their morphology. They found that 80 and 160 $\mu J/cm^2$ THz radiation demolished actin filaments, while actin aggregation was present near the cell after a 250 $\mu J/cm^2$ irradiation [28].

Since the reaction rate of the actin polymerization is temperature-dependent, there is the possibility that increased temperature of water due to absorption of THz waves could explain reduced actin filaments. To test this hypothesis, they measure the sample temperature at the end of the irradiation. It was 1.4°C higher than the control. Actin polymerization does not produce noticeable results until temperatures above 50°C. Therefore, temperature increases of a few degrees Celsius do not explain the inhibition of the polymerization reaction [28].

2.3.1.3. Tubulin

THz radiation was documented to cause MTs disassembly, but no clear explanation of this process is available yet [18]. Conformational changes that convert to structural instability (similar to the effect of colchicine drugs) and GTP hydrolysis to GDP (hypothesised behaviour of Taxol) are two viable hypotheses behind MTs disassembly.

Raman analysis can help us narrow down the solution.

2.4. Raman spectroscopy

Raman spectroscopy is an effective label-free method for analysing chemical species in biological samples. Large shifts in Raman band positions, also known as frequency shifts, can be caused by changes in molecular geometry, particularly conformational transitions found in biological macromolecules, allowing the technique to be used to diagnose protein secondary structure, determine side-chain configurations, and detect interacting side-chain groups [29]. Indeed, the peaks within the weakly scattering Raman fingerprint region (< 1,800 cm^{-1}) are used to discriminate subtly different states of cells and tissues [30]. In particular, the amide bonds which link amino acids can be classified primarily as Amide I, Amide II and Amide III.

The Amide I band (1600–1700 cm^{-1}) is a signature region for C=O stretching/N-H bending, and N-H bending/C-N stretching vibrations [1], [31].

The Amide II band (1510–1580 cm^{-1}) also gives information on the protein backbone's vibrational bands. However, it is primarily derived from in-plane N-H bending (40–60% of the potential energy) and C-N stretching (18–40%), with minor contributions from C=O bending and C-C stretching vibrations, resulting in less sensitivity and specificity for protein conformational changes when compared to the amide I band. Indeed, the Amide II band has a relatively small Raman cross-section under non-resonant conditions, making it invisible in protein Raman spectra [31], [32].

The Amide III range (1220-1310 cm^{-1}) is mostly attributable to N-H in-plane bending and C-N stretching [33].

These three bands can be exploited to make quantitative estimates of a protein's secondary structure [1], [31]. The most common secondary structures observed are the α-helix, the beta (β) sheet, loops, turns, etc.

The α-helix is stabilized by the hydrogen bonds between the carbonyl (–C=O) groups of each peptide bond parallel to the axis, and the N–H group of the peptide bond of the amino acids below in the helix [34].

The β-sheet structures, on the other hand, is extended. This is not the only distinction between the two mentioned secondary structures. A few polypeptide chains are required to produce the β-sheet (at least two interacting with each other via H-bonding), while just one is enough for the α-helix. The β-sheet has the greatest diversity of functions among all secondary protein structures. β-sheets can be categorised into many configurations. Parallel and antiparallel forms are the most well-known β-sheet structures. The position of the polypeptide chains in the same direction produces a parallel β-sheet form, while the orientation in the opposite direction produces an antiparallel form [34], [35].

Amide I and Amide III Raman bands - Amide I in particular - are especially useful for determining peptide backbone conformations in proteins. Indeed, the Amide I band has been shown to be the most sensitive and widely used band for studying protein secondary structure [31].

Proteins with a high α-helical composition usually have an amide I band in the 1645-1658 cm^{-1} range and an amide III band in the 1260-1310 cm^{-1} range. Proteins with a predominant β-sheet and/or random coil structure, on the other hand, show an amide I peak at 1660-1680 cm^{-1} and an amide III band at 1230-1260 cm^{-1} [33]. Many studies report slightly different ranges, for example, Sadat et al. consider, typical wavenumbers for α-helix and random coil conformation, in the Amide I band, 1649–1660 cm^{-1} and 1660-1665 cm^{-1},

respectively. They identified two different ranges of the Amide I band belonging to β-sheet structures (1620-1648 and 1665-1680 cm^{-1}), while bands centred between 1680 and 1699 cm^{-1} were assigned to β-turn assemblies [31]. We are going to use this latter distinction to identify our peaks.

Recently, Kuhar et al. discovered that a helix of six or more residues produces a distinct Amide I band at 1655 cm^{-1}. While, helices composed of less than six amino acids, instead of a single recognisable peak, have several peaks and the corresponding amid I band shifts down as the helix length grows [32]. Furthermore, when the α-helix is well-formed, tight peaks appear, which become broader as the structure becomes less well-formed [36].

The position of the amide I band in β-sheets is determined by the number of strands rather than the number of residues. A reduction in the number of strands - from 12 to 1 - results in a significant red-shift of the Amide I peak for β-sheets [32], [37].

Finally, as already mentioned, the amide III vibration is also affected by peptide conformation. A β-pleated sheet has a strong feature at 1230–1240 cm^{-1}, whilst the disordered structure is highlighted by a broadband near 1240–1245 cm^{-1}. However, based just on line, shape and intensity, it is difficult to distinguish the disordered form from the β structure [34]. Slightly different values are reported in different articles. For example, for Ishizaki et al. and Bhattacharya et al., the three key secondary structures β-sheet, disordered structure, and α-helix of a protein contribute in the ranges 1235-1242, 1242-1250, and 1260-1310 cm^{-1}, respectively [38], [39].

Raman in the amide III area is thought to be the most conformationally sensitive band, even though this band analysis is complicated by overlapping bands caused by side-chain vibrations [35], [36]. In-phase combinations of the Cα-H bend with the amide III N-H bend produce a strong Raman band centred around 1235 cm^{-1}, but out-of-phase combinations produce two weaker bands between 1300 and 1400 cm^{-1}. The Cα- H bending contributes substantially to the smaller peak near 1400 cm^{-1} [35].

Protein Raman spectra typically have sharp features due to aromatic ring modes [36].

Raman spectra we are going to look at are Actin and Tubulin spectra. It is possible to find many references about the actin spectrum [40]–[44], while there is little knowledge about tubulin [1], [45]. In this regard, studying tubulin secondary structure, Audenaert et al. demonstrated that it is possible to distinguish between GDP and GTP-tubulin bound states. Indeed, the key differences between GTP and GDP include an increase in the antiparallel β-sheet at the expense of the ordered α-helix, while the disordered helix content stays unchanged [1]. As previously mentioned, Raman analysis can help us estimate the amount of secondary structures present in our samples and therefore, help us distinguish these two conformations.

Several results in the literature show that there is significant overlap between parallel and antiparallel sheet scattering and that Raman spectroscopy cannot distinguish between these two structure types, indeed their centre components at 1670 cm^{-1} are the

same in both forms [35], [46]. The same goes for the Amide II band where both β-sheet types are quite weak and essentially featureless. Finally, their intensity variations in the Amide III band, particularly at 1330 1300 cm^{-1}, can be detected, although these differences are unlikely to be significant enough to provide a reliable way of structural discrimination [35]. A better way to differentiate parallel and antiparallel β-sheet is polarization-controlled two-dimensional (2D) IR (infrared) photon echo spectroscopy [47].

The other type of exposure we are going to investigate involves Vielight devices.

2.5. *Vielight*

Although photobiomodulation (PBM) therapy, originally known as low-level laser therapy (LLLT), was discovered more than 50 years ago, there is still no agreement on the parameters and protocols for its clinical application [48]. PBM is based on the use of red or near-infrared (NIR) light to heal, restore, and stimulate physiological processes, as well as to repair damage caused by injuries or diseases. Nowadays the interest in using PBM in oncology is growing. However, there are many contradicting findings when it comes to the utilisation of this form of treatment because no clear methodology has been identified yet [49], [50]. Under some conditions, LLLT may promote tumour cell proliferation. On the other hand, other studies reported improvement of wound healing while reducing pain, tissue swelling, and inflammatory disorders such as radiation dermatitis (RD), oral mucositis (OM), and lymphedema. Following this second tread, LLLT may be used in conjunction with tumour treatments to mitigate their side effects. Indeed, RD and OM are well-documented complications of radiotherapy (RT) [50], [51]. Cialdai et al. stated that the behaviour of cancer cells is greatly influenced by the cell type, the treatment parameters utilised, and the administration manner. Therefore, using a treatment on cancer patients requires extreme caution and additional research: each unique application necessitates a careful selection of the source as well as a thorough assessment of its effects on appropriate cellular and animal models [52]. Many reviews tried to shed light upon this controversy.

Del Vecchio et al. takes on PBM is that it may play a beneficial role in treating cancer patients, but further evidence about its clinical efficacy and the identification of protocols and correct dosages is still needed. They, together with others [53], asserted that PBM, like conventional drugs, follows the rules of the "biphasic dose-response" curve, also known as the Arndt–Schulz curve, or the hormesis phenomenon. According to this theory, there are ideal parameters that benefit irradiated tissues, but if these values are severely exceeded, irradiation might cause harm [49]. Indeed, according to the Arndt-Schulz Law, mild stimuli moderately increase vital activity, stronger stimuli raise it even more until a peak is reached, and even greater stimuli lower vital activity until a negative response is produced [54]. However, while the biphasic dose-response is widely acknowledged in normal tissue, it is unclear how it translates to cancerous tissue. In some cases, a very high dose appears to produce a cytotoxic level of reactive oxygen species (ROS) capable of directly destroying the tumour. In other circumstances, a low dose may be more effective since PBM's main function could be to boost the immune system [55].

There are two types of parameters that can be defined. The wavelength (nm), power (W), beam size (cm^2), and pulse structure of the irradiation are all connected to the light source. The dose parameters, on the other hand, such as energy (J), energy density (J/cm^2),

treatment repetition, and irradiation time (s) and area (cm^2), are all regulated by the operator [56].

The most important ones are the power density (irradiance) measured in mW/cm^2 and the energy density (fluence) measured in J/cm^2 [48]. We will be addressing the dose in terms of energy density. PBS is typically delivered with power density which varies between 5 and 150 mW/cm^2 and energy density values that range from 0.1 to 12 J/cm^2 [51]. Some groups suggest up to 50 J/cm^2 at the tissue surface. Other investigations found that the desired increased proliferation at the cellular level was obtained at fluences values ranging from 3 to 10 J/cm^2 [48]. There is still no defined protocol, as previously stated.

Literature reports that PBM is typically in the red and near-infrared (NIR) wavelength ranges of 600 - 1000 nm [51]. Cell proliferation was shown to be most affected by light in this range. Shorter wavelengths are absorbed by haemoglobin or melanin, while longer ones by water, allowing only light in this "optical window" to reach the cells [49], [50].

2.5.1. *Cellular mechanisms*

Under hypoxic conditions or in stressed cells, mitochondria produce nitric oxide (NO), which binds to cytochrome c-oxidase (COX) in the respiratory chain and displaces oxygen. The consequences are reduced adenosine triphosphate (ATP) synthesis, suppression of cellular respiration, and increased oxidative stress [51].

It is worth noting that, as tumour cells grow, blood vessels become constrained, disordered, and non-functional, resulting in insufficient tissue irrigation, and consequently in a lack of oxygen (hypoxia) and nutrients. Indeed, in cancer cells, acidic pH and a shortage of oxygen are always significantly related to malignancy [57].

Evidence suggests that when PBM is given to stressed cells with the right parameters, ATP generation increases, NO is detached from its competitive binding to COX, and the balance between pro- and antioxidant mediators is restored [51]. Indeed, increased NO concentrations were measured in cell culture or animals after LLLT. As a result, PBM could play a key role in restoring proper respiratory chain activity and reversing the mitochondrial inhibition of respiration caused by excessive NO binding [53]. It is well established that cancer cells switch their metabolism from oxidative phosphorylation (OXPHOS) to glycolysis even under proper oxygenation levels [58]. This is known as the "Warburg effect," which was discovered by Otto Warburg and garnered him the Nobel Prize in Physiology in 1931 [59].

The hypothesis of the mode of action of PBM is that the photons emitted reach the inner mitochondrial membrane, where they interact with COX. The energy of visible red-light photons at a low-fluence is sufficient to separate NO from COX and increase COX reduction capability, resulting in cancer stem cells (CSC) proliferation via ATP, cyclic adenosine monophosphate (cAMP), and mild ROS generation. Through this method, PBM promotes growth factor synthesis and improves the motility and viability of irradiated cells. In contrast, the energy of photons supplied by visible high-fluence red light is sufficient to reduce COX reduction capacity, resulting in a large conversion of dioxygen to ROS and programmed cell death. Indeed, a considerable increase in both viability and proliferation in CSCs was seen when low fluences of 5, 10 and 20 J/cm^2 were used with wavelengths between 600 and 800 nm. On the other hand, exposure to 40 J/cm^2 resulted in a statistically significant reduction in viability and proliferation, as well as an increase in apoptosis [49]. This hypothesis highlights an energy density dependence and agrees with Tam et al. findings that LLLT

indeed promoted cell proliferation, but with an inverse correlation between LLLT power (or energy) density and cellular responses. Greater energy density resulted in more inhibited cell proliferation, migration, viability, and ATP activity [50].

Vielight effect on tubulin has not been documented yet. However, unpublished results (known through personal communications) witnessed how MTs polymerisation was slowed down after exposure.

2.6. Turbidity measure

In this regard, a useful tool to assert MTs polymerisation is turbidity measure. Turbidity assays have been used to identify novel compounds which are potentially useful in anti-cancer applications since, as before mentioned, MTs and tubulin are important targets for many drugs.

Because it is easy, requires no special equipment, and is quantitative, turbidity is the most extensively used method for following tubulin polymerization. A spectrophotometer and an optically clear vessel (cuvette or multiwell plate) are all that is required. The resulting turbidity data can be used to make quantitative measurements of assembly kinetics and steady-state polymer concentrations.

A lag time, a period of net growth, and a steady-state (characterized by a plateau). describe tubulin assembly. An elevation in the amount of polymerized tubulin is accompanied by an increase in the curve's maximum slope and plateau.

The lag period (the time before the OD begins to rise), the maximum rate of OD increase, and the OD reached at steady state are the three curve characteristics to analyse. These variables are frequently deeply correlated, but they do not have to be.

The lag time is usually proportional to the number of nucleation events, which influences the number of MTs (more nucleation events mean more short MTs), but not necessarily the overall quantity of polymer generated. Even though the total mass of MTs is the same (two different curves settle to the same plateau value), a shorter lag phase could suggest an increased number of nucleation events causing an increased number of shorter MTs [60].

3. Materials and methods

3.1. *Tubulin reconstitution*

Unlabelled tubulin, purchased from *Cytoskeleton, Inc.* (T240), was employed in the following experiments.

3.1.1. Unlabelled *tubulin*

T240 were stored at 4°C and lately reconstituted to 2,5 mg/ml tubulin by adding to each vial 360 ul of GPEM buffer and 40 ul of Microtubules Cushion buffer. The GPEM buffer was previously prepared by adding 590 ul of Brinkley Renaturing Buffer 80 (BRB80) and 10 ul of GTP 100mM; therefore, the GTP final concentration of the GPEM buffer is 1mM. After reconstitution, the samples were aliquoted in experimental amount and freeze-dried through immersion in liquid nitrogen to avoid protein denaturation. Finally, the samples were stored at -80°C.

3.1.2. Paclitaxel *and CCI-001 administration*

CCI-001 was provided by the Department of Oncology, University of Alberta (Edmonton, Canada), while the Taxol was purchased from Cytoskeleton, Inc. (TXD01). To administrate these drugs, GPEM-P and GPEM-C were respectively created adding 1ul of Paclitaxel or CCI-001 to 500ul of GPEM. In this case, unlabelled tubulin was reconstituted by adding to each vial 360 ul of GPEM-P or GPEM-C buffer and 40 ul of Microtubules Cushion buffer. The same storing procedures as the previously mentioned samples were applied.
The different drug concentrations are reported in Table 1.

Table 1. *Drugs concentrations*

Drug	**Initial concentration**			**Final concentration**		
Taxol	2 mM			3.59 µM		
CCI-001	2 mM	10 mM	10 mM*	3.59 µM	18 µM	225 µM

*In this case, a different amount of the initial CCI-001 stock was utilized: 10.2564 µl of CCI-001 10mM were added to 400 ul of GPEM to create 250µM GPEM-C buffer. As before, 360 µl of GPEM-C buffer were added to 40 µl of Microtubules Cushion buffer and a tubulin aliquot to achieve a CCI-001 final concentration of 225µM.

3.2. *Cell lines*

Cells were provided by the Lewis Lab. (Katz Building - Alberta, Edmonton, Canada). They were kept in 75 cm^2 Falcon culture flasks at 37°C under conventional culture conditions of 5% CO_2 in air with medium replacement every 2–3 days, depending on the cell line. Cells were cultured in Dulbecco's Modified Eagle Medium (DMEM) high glucose, with 10% fetal bovine serum (FBS) and 1% Penicillin-Streptomycin (PS), in normal condition and were split when confluent. Synchronization was obtained through serum starvation.

Three different cell lines were cultured and evaluated in this project. MCF7 breast cancer cell line, A2058 melanoma cell line. The cell lines were chosen based on previous studies (MCF7), to be able to compare results, and on the possibility of reaching the cells with radiation (A2058). Indeed, during in vivo treatments, attenuation must be considered.

3.3. *Turbidity measure*

To perform turbidity analysis, the tubulin samples were collected from the -80°C freezer, thawed on ice, and quickly pipetted into a 96 well plate. The plate was then read using the *SpectraMax iD5* microplate reader (Figure 5) in 340nm absorbance kinetic mode for 40 minutes. 81 points were collected, one every 30 seconds. Between reading the plate was shacked. All parameters are reported in Table 2.

Figure 5. *SpectraMax iD5 microplate reader*

Table 2. *Microplate reader parameters*

Parameters	Setting
Measurement mode	Kinetic, 81 cycles of 1 reading per 30 seconds
Absorbance wavelength	340 nm
Temperature	37°C
Shanking	5s medium, orbital
Designation of blank	Blanks are not assigned. The first value is automatically set to zero.

3.3.1. Data Analysis

The data collected were analysed using the Software OriginLab. To perform outlier removal, the curves were filtered with a FTT filter with 5 points of window and a cut off frequency of 0,0033. The data were fitted with Boltzmann sigmoidal curve to obtain their slope and plateau values. Finally, the lag time was calculated by determining the tenth time,

$t_{1/10}$ (the time required to produce 10% of the final amount of polymer), as done by Bonfils et al. [61].

3.4. *Raman Spectroscopy*

Raman spectra were acquired with the 532nm laser, 1200 lines per mm grating, 100% power, exposition time 1s, using the *Renishaw inVia Raman microscope* (Figure 6). The 50L magnification was used to focus the samples. Multiple acquisitions (4/5) were made for each point, and multiple points of the same samples were analysed.

Figure 6. *Renishaw inVia Raman microscope set-up*

3.4.1. THz exposure

T240 samples, in powder form, were exposed to THz for 30 minutes and read 1 hour or 24 hours after the exposure. Exposure parameters are reported in Table 3. Two timepoints were used to determine whether the effect of the radiation was persistent in time. Each sample had its control.

Table 3. *THz exposure parameters. The beam spot is an ellipsis with x-axis width (wx) and y-axis width (wy)*

Parameters	**1st exposition**	**2nd exposition**
Peak field (kV/cm)	200	190
Pulse Energy (μJ)	1.28	1.27
Peak Intensity average (mW/cm^2)	37.47	
Peak Intensity Max (MW/cm^2)	28.43	
Pulse duration (ps)	1.32	
Peak frequency (THz)	0.76	
Beam spot size (wx x wy mm^2)	2.29 x 2.07	

3.4.2. Data processing

The data were processed through the software OriginLab.

After the acquisition, Range reduction and baseline corrections were implemented. An asymmetric least squares smoothing with a 0.05 threshold, a smoothing factor of 5 and 10 iterations were employed for baseline correction. The data were smoothed using Savitzky-Golay with 20 points of window and normalized between 0 and 1. Peaks deconvolution was performed with Gaussian function using the 'Peak Deconvolution' tool by

OriginLab Technical Support and their analysis was carried out through literature research as previously described.

Following the fitting procedure, the amide I vibrational peak areas were used to evaluate the protein's secondary structure content. This analysis was carried out by simply adding the areas of all Amide I peaks and calculating the individual contribution of each peak (α-helices, β-sheets, turns, and so on). This method is suitable because the Raman absorption cross-section for these multiple types of delocalized vibrations in a given protein is the same.

3.5. *Laser irradiation*

The exposure was done with the Nasal applicator of the 'Neuro Alfa' device which parameters are reported in Table 4. The experiments were carried out in triplicate.

Table 4. Characteristic parameters of the Nasal applicator of the Vielight 'Neuro Alfa' device

'Neuro Alfa' nasal applicator		
Parameters	Source	LED
	Wavelength (nm)	810
	Power density (mW/cm^2)	25
	Pulse frequency (Hz)	10
	Pulse duty cycle	50
	Beam spot size (cm^2)	1

3.5.1. Tubulin

Tubulin samples were collected from the -80°C freezer and place inside the 4°C fridge to perform the exposition. To avoid repositioning of the sample with respect to the LED, it was taped to the nasal applicator and finally to a cardboard box. The box is also utilized to keep the sample in the dark during exposure to avoid light diffusion and reflection. Finally, the exposed sample was then kept inside the 4°C fridge until a triplicate was prepared.

3.5.2. GTP

We exposed an aliquot of 10µl GTP (100mM) to reconstitute tubulin following the same procedure outlined in Section 3.1.1. The purpose of this experiment is to understand at which point of the process the tubulin is modified by the exposure. On the same line of thought, formed MTs were also exposed.

3.5.3. Microtubules

Tubulin samples were collected from the -80°C freezer and place inside the incubator at 37°C to achieve polymerisation. After one hour, MTs were formed and exposed to the Vielight device. Similarly to before, the exposed sample was taped to a stand to avoid repositioning. The incubator allows both fine temperature control and to keep the sample in the dark. In this case, we exposed altogether a 400µl aliquot.

3.5.4. Actin

Actin reconstituted samples, stored at -80°C, were provided by the Lewis Lab. The exposure procedure traced MTs exposure.

3.5.5. Cells

The nasal applicator was taped to the bottom of the 96-plate using some cardboard pieces. A stand was created out of other carboard to let the plate rest horizontally. Before each stimulation, the correct positioning of the device could be assessed by looking through the top of the plate. The set-up for the experiment can be seen in Figure 7. The surface area of each well was 0.32cm^2, smaller than the beam spot size: the entirety of the surface was irradiated. Once the treatment started, the plate was placed inside the incubator to maintain the cells at the correct temperature, within a suitable environment, and to keep them in a dark space.

The exposure time was decided to depend on the desired delivered dose. The energy density range was chosen to include the most reported literature values. Each time point and correlated dose are reported in Table 5. Non-irradiated cells served as the control.

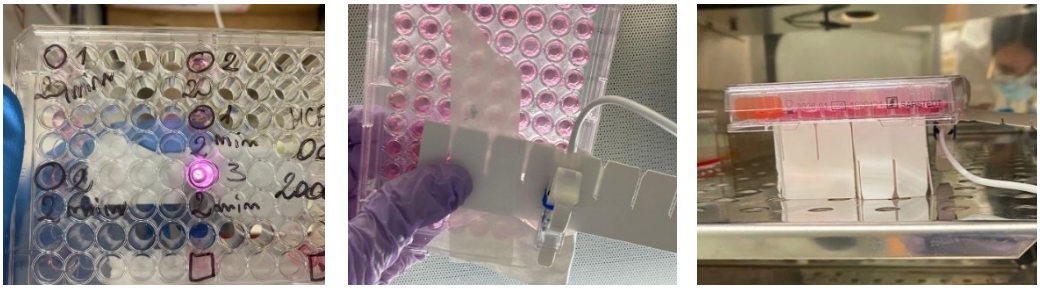

Figure 7. *Vielight cells exposure set-up*

Table 5. *The energy density (J/cm^2) values calculated knowing the duty cycle (DC) is 50% and the LED power density is 25mW/cm^2.*

Exposure (min)	The energy density (J/cm^2)
CTRL	0
2	1.5
20	15
60	45

To summarize, Vielight exposure parameters are reported in Table 6.

Table 6. *Vielight exposure settings employed in each experiment*

Sample	Unlabelled tubulin	GTP	MTs	Actin	Cells
Exposure length	30 min 2 h	30 min	30 min	30 min	30 min
Temperature	4°C	4°C	37°C	37°C	37°C

3.6. *Cells counting*

Viable cells were counted in a hemacytometer chamber using a 1:5 proportion of Trypan Blue (5% in PBS) in DMEM at the beginning and the end of each treatment. 2000/1000 cells per well were seeded in a 96 wells plate – for MCF7 and A2058 respectively, due to their different doubling times. To each well was added 100µl of DMEM and the cells were left overnight to attach. In some cases, cells synchronization was achieved via 24 hours starvation.

3.7. *Proliferation assay*

After the stimulation, the proliferation was evaluated by the AlamarBlue® assay, which is not toxic to the cells so they can be evaluated multiple times for several days [62]. Indeed, the AlamarBlue® Cell Viability Assay Reagent is used to quantify cellular metabolic activity and in turn determine the concentration of viable cells in a given sample.

We removed the present medium inside the wells and replace it with 100µl of 10% Resazurin in DMEM and filled in three wells without cells to use as a control. The plate was left to rest in the incubator for 4-5 hours. Finally, a fluorescence read was performed with the *Fluo star Omega* device at 544/590 nm wavelengths.

Afterwards, the medium was removed, and each well was washed with 100µl of phosphate-buffered saline (PBS). Finally, 100µl of DMEM was added to each well and the 96 plate was stored in the incubator for the next-day treatment. The stimulation was repeated for 7 days or until cells confluence was reached.

3.8. *Statistical Analysis*

The data collected were analysed using the software Excel, and GraphPad Prism 8.0.1.

Through Excel, the fluorescence of the media was mediated and then subtracted from both the exposed wells and the controls. Afterwards, each fluorescence well value was divided by the mean of the controls first-day detection.

The data were then imported to GraphPad where multiple comparison 2way ANOVA test was performed, and graphics were created.

4. Results

4.1. *Turbidity measure*

Multiple turbidity measurements were performed exploiting both Vielight irradiation and drugs administration. The measures in kinetic mode were conducted for a minimum of 40 minutes and each curve was fitted with a sigmoidal model (OriginLab report can in found in the supporting information). At least three samples were employed to create every curve (figures will display mean values and standard deviations).

4.1.1.1. Vielight

Different unlabelled tubulin concentrations brought different outcomes; therefore, we are going to analyse them in separated sections, starting with the less concentrated tubulin.

4.1.1.2. 2,5 mg/ml tubulin

In figure 6.a are reported the control and exposed curve for 2,5 mg/ml tubulin. We fitted the data with Boltzmann curves (Figure 6.b) to analyse their differences. The curves have different lag times (870 Control and 990 s Exposed), distinct slope (Control: 4,476 ± 1,039 mOD/min, Exposed: 3,131 ± 0,604 mOD/min) and reach different plateau values (respectively 0,087 ± 3,64e^{-4} and 0,074 ± 5,65e^{-4} for control and exposed).

4.1.1.3. Exposed GTP

In this case, the curves were filtered with a FTT filter to perform outlier removal (5 points of window and a cut off frequency of 0,0033). Consistent with before, the lag times are slightly different: 810 s for the controls and 900s for the exposed. The slopes for these curves are 5,122 ± 0,731 mOD/min (Control) and 4,754 ± 0,484 mOD/min (Exposed) (Figure 8.d). Initially, the curves (Figure 8.c) followed the same trend, but the samples reconstituted with the exposed GTP settled to a higher plateau value (0,107 ± 3,47e^{-4}) with respect to the control (0,091 ± 2,49e^{-4}). This behaviour is the opposite of the previous experiment.

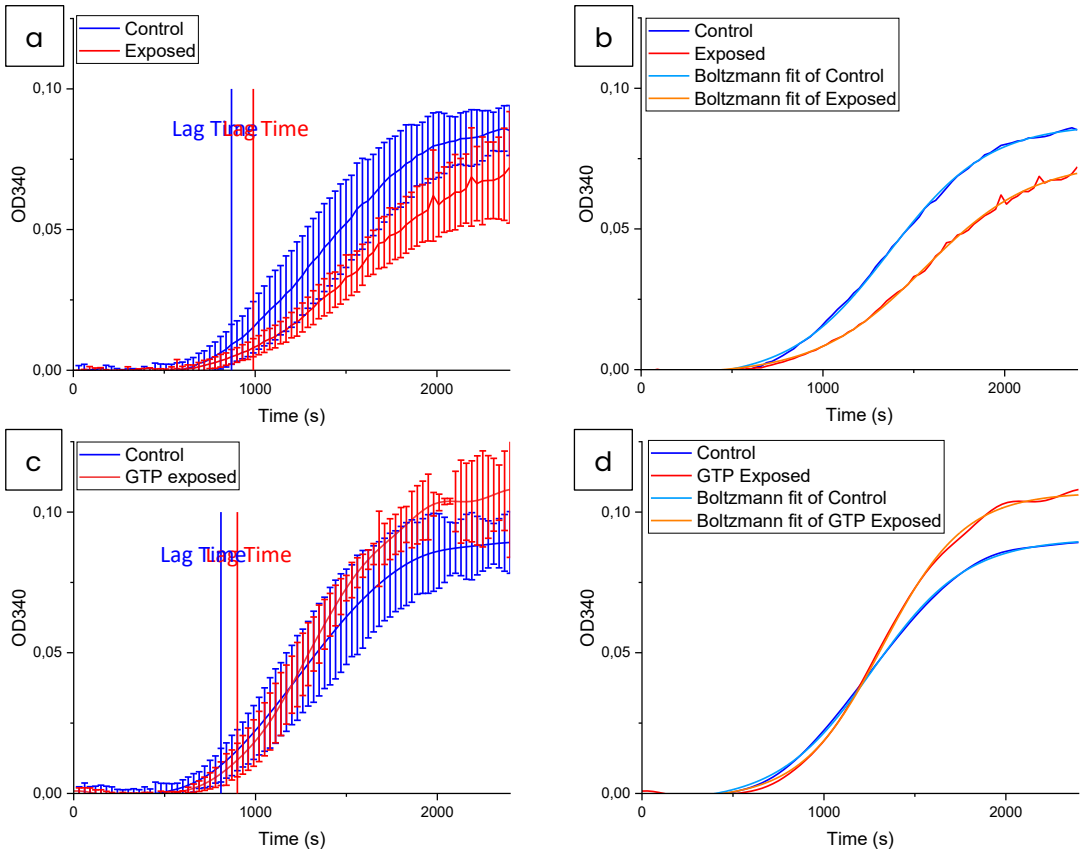

Figure 8. *Turbidity measure of* ***a.*** *Vielight exposed (red) and unexposed (blue) 2,5 mg/ml tubulin: average and standard deviation* ***b.*** *Relative Boltzmann fitted curves* ***c.*** *exposed GTP reconstitute 2,5 mg/ml tubulin (red) and control (blue) and* ***d.*** *relative Boltzmann fitted curves*

4.1.1.4. 2,5 mg/ml Microtubules

As explained previously, MTs were also exposed in order to determine when or how the protein was impacted during the polymerisation process. The mean and standard deviation of the triplicate of experiments are shown in Figure 9. This time, the Vielight exposure increased the number of MTs formed.

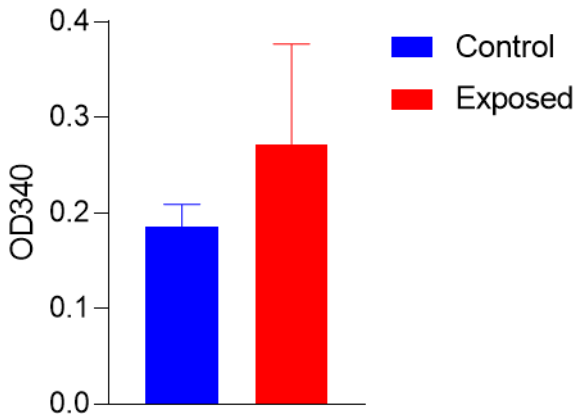

Figure 9. *Endpoint turbidity measure of exposed MTs*

4.1.1.5. 2,5 mg/ml tubulin – 2h exposure

Tubulin exposed for a longer time presented different turbidity trends (Figure 10.a). In this situation, the curves present a larger standard deviation that overlaps for the most part; therefore, an analysis of the two averages will not give any significant information.

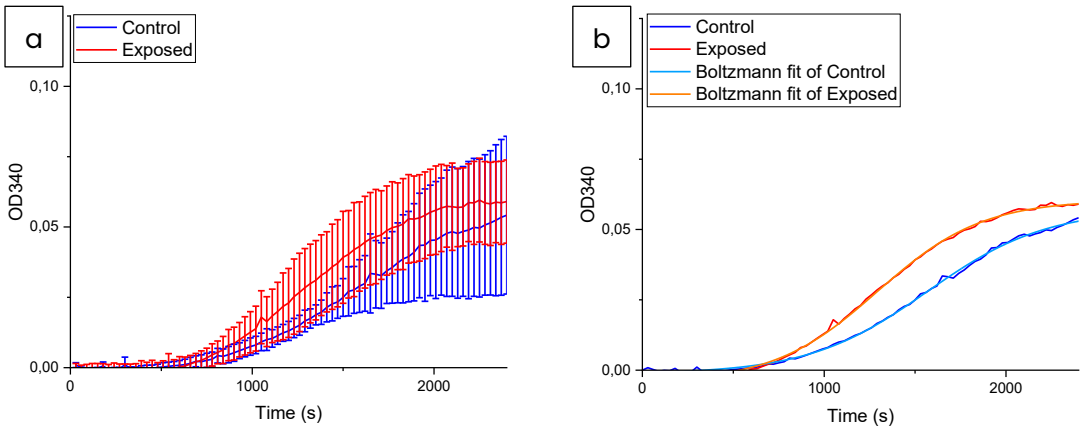

Figure 10. *Turbidity measure of* ***a.*** *2h Vielight exposed (red) and unexposed (blue) 2,5 mg/ml tubulin: average and standard deviation* ***b.*** *Relative Boltzmann fitted curves*

4.1.1.6. 5 mg/ml tubulin

In Figure 11.a are reported the turbidity curves for the 5 mg/ml unlabelled tubulin. In this instance, the curves lag time are 480s for the control and 420s for the exposed. Their polymerisation rates were 2,196 ± 0,581 mOD/min for the control and 3,195 ± 0,638 mOD/min for the exposed (Figure 11.b). Finally, the control had a plateau value of 0,140 ± 4,02e^{-4} while the exposed samples settled to 0,181 ± 3,94e^{-4}.

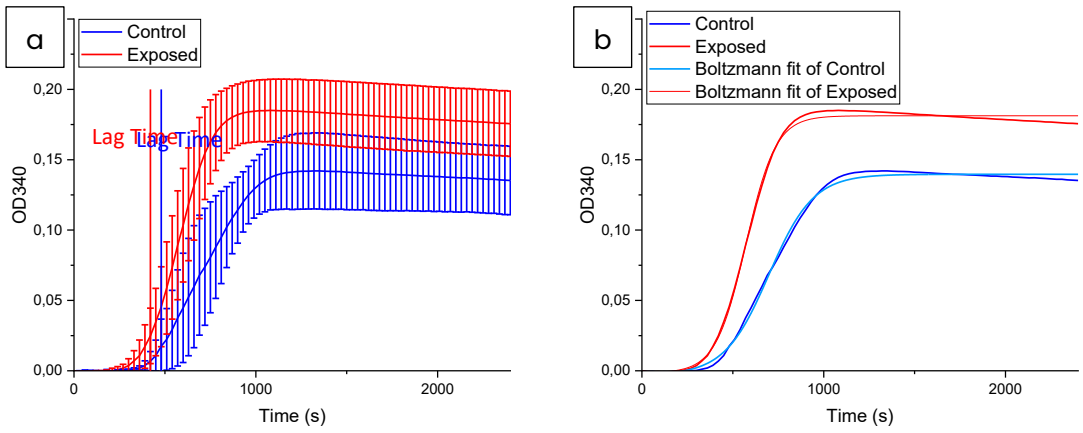

Figure 11. *Turbidity measure of* ***a.*** *Vielight exposed (red) and unexposed (blue) 5 mg/ml tubulin: average and standard deviation* ***b.*** *Relative Boltzmann fitted curves*

4.1.1.7. Taxol and CCI-001

Figure 12 shows the effects of 3.59 µM Taxol and different concentration CCI-001 (respectively 3,59 µM in light green, 18µM in dark green and 225 µM in teal) on MTs polymerisation starting from 2,5 mg/ml unlabelled tubulin.

In this case, the Vmax value is 15,272 ± 0,467 mOD/min for the Taxol curve and 3,764 ± 0,509 mOD/min for the control.

3.59 and 18 μM CCI-001 cause a prolongation of the nucleation phase and induce a 2-fold reduction in final polymer mass, with respect to the control. When 225 μM CCI-001 is administered, however, a different result is achieved. The curve grows with a polymerisation rate greater than the control. Further analysis may be required due to the large standard deviation.

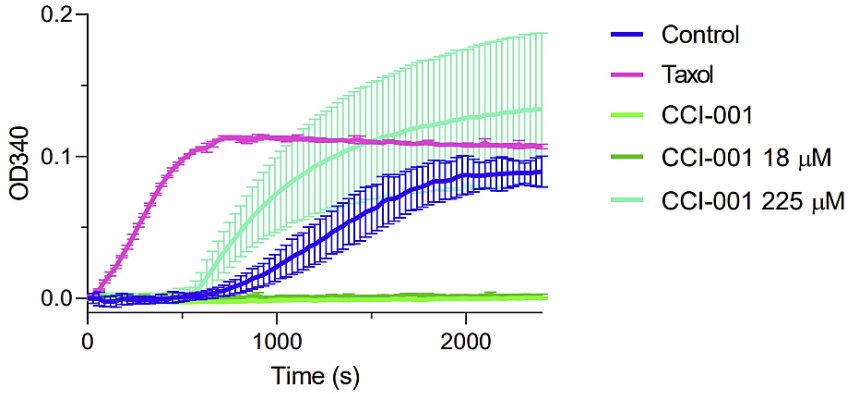

Figure 12. Turbidity measure of forming microtubules in presence of 3,59 μM Taxol (pink) and different concentration of CCI-001 (3,59 μM light green, 18μM dark green, teal 225 μM). The control is displayed in blue.

4.2. Raman analysis

Raman spectroscopic investigation was carried out as it can reveal structural changes in tubulin and MTs after their interaction with Vielight and THz emissions.

4.2.1. Vielight

Proteins were exposed to Vielight for 30 minutes – as described in Section 3.5 - and were left polymerised for 60 minutes inside the incubator. We are going to refer to these samples as 'Exposed Polymerised'. On the other hand, we will be referring to the polymerised and then exposed samples as 'Polymerised Exposed'.

4.2.1.1. Actin

As a reference, we are going to look up the Actin spectrum provided by Silveira et al. in their work (Figure 13) [43].

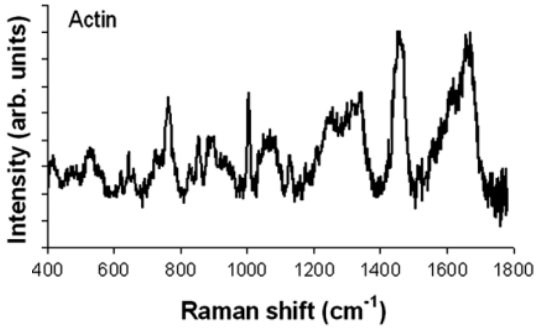

Figure 13. *Raman Spectroscopy spectrum of actin. This image is displayed with the permission of ref.* [43]

In Figure 14 are reported our Actin spectra (350-2700 cm^{-1}) with and without Vielight exposure. Although some peaks present different amplitudes, our control curve generally follows the literature trend.

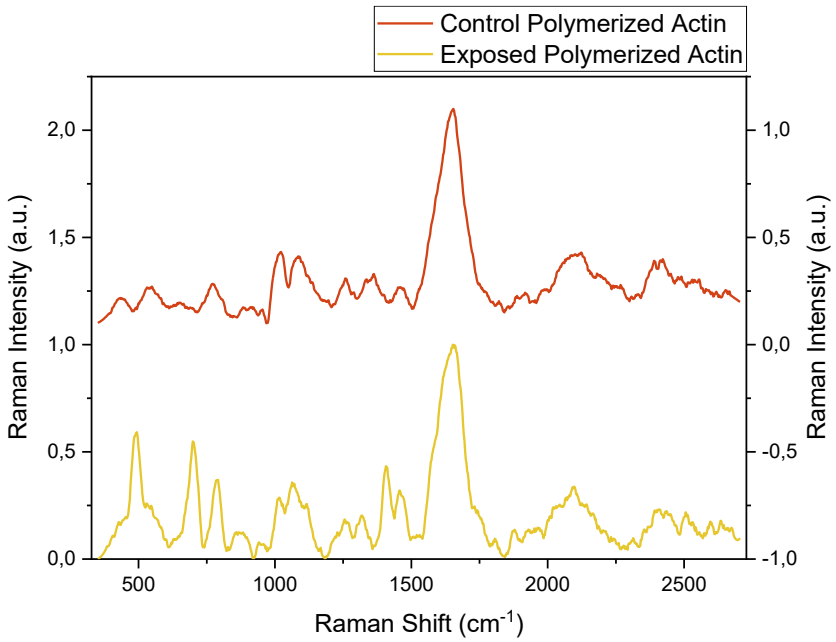

Figure 14. *Raman Spectroscopy spectra of Vielight exposed and unexposed actin*

The regions under the Amide I band were used to calculate the relative quantities of actin secondary structures. We fitted the spectrum within 1580-1750 cm^{-1} with Gaussian function using the 'Peak Deconvolution' tool by OriginLab Technical Support (Figure 15). Further info about the fitting can be found in the Supporting Information.

As per Control Polymerised Actin, a 1655 cm^{-1} peak was identified and classified as an α-helix peak. The exposed sample, on the other hand, presented two peaks within the Amide I region at respectively 1633 cm^{-1} and 1671 cm^{-1}, both belonging to β-strand structures. The fittings are reported in Figure 15.

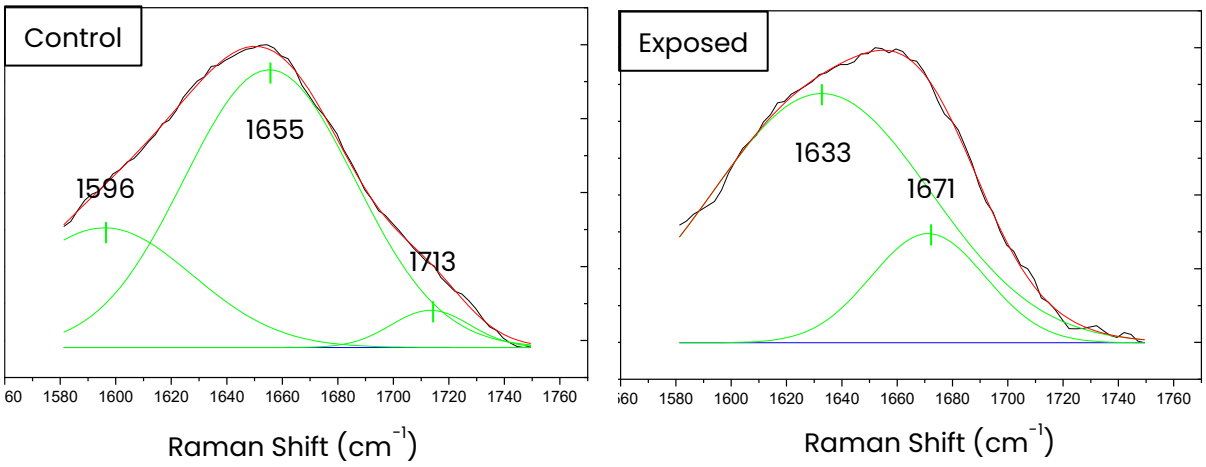

Figure 15. *Peak Deconvolution of the Amide I band of Control and Exposed Actin*

4.2.1.2. Tubulin

As before mentioned, there are not many references about the Raman spectroscopy tubulin spectrum. We are going to use Piyush Kar (University of Alberta, Edmonton) work (Figure 16). As additional references, Choudhury et al [45] presented tubulin and MTs (100-1800 cm^{-1}) spectra and Audenaert et al. [1] provided the Amide I spectra of tubulin of pure tubulin with 1 mM GTP and tubulin in the presence of 1 mM GDP at 4°C.

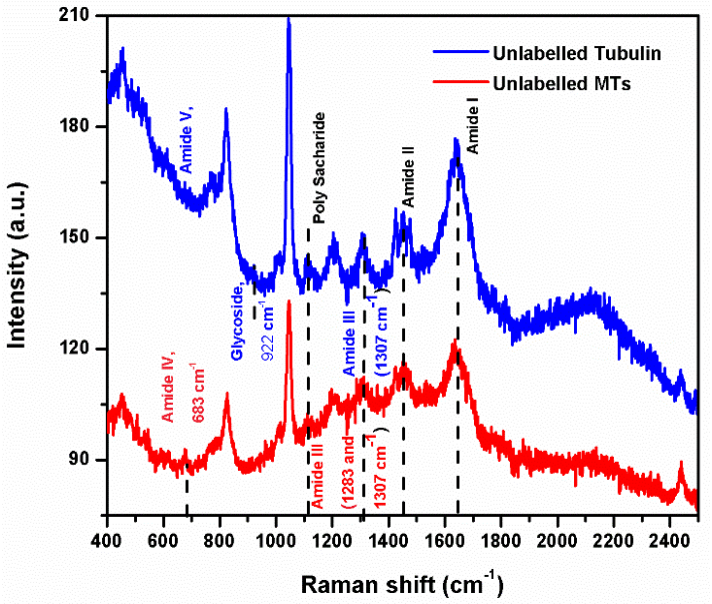

Figure 16. *Raman Spectra of tubulin and MTs. This image is displayed with permission of Piyush Kar*

We obtained 'Exposed Polymerised' and 'Polymerised Exposed' tubulin spectra reported in Figure 17, as well as the control curve which represents Microtubules.

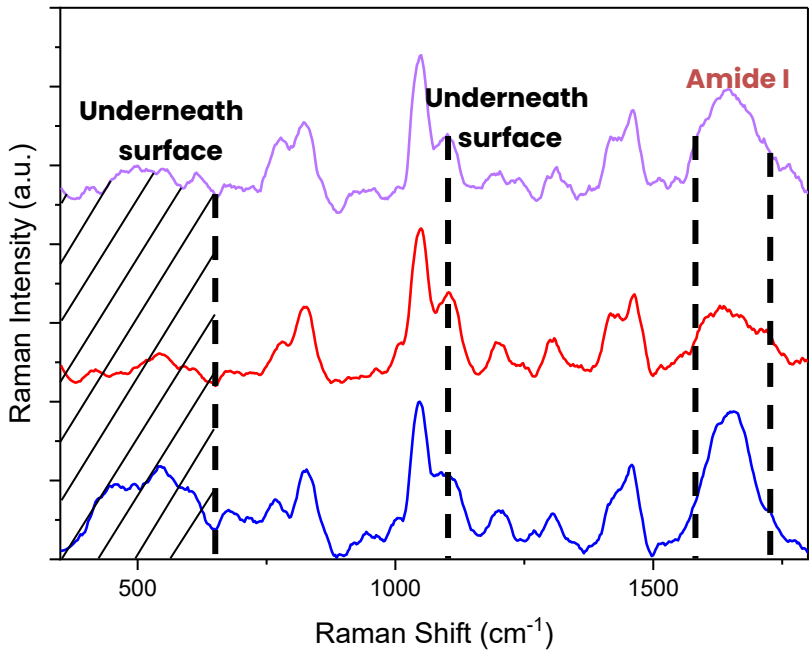

Figure 17. *Raman spectra of polymerised tubulin solutions. Blue curve: Control; red curve: Polymerised Exposed sample; Lilac curve: Exposed Polymerised sample*

It is possible to witness the presence of the surface underneath the samples by some peaks present in the range around 400-700 cm^{-1} and a sharp peak centred at 1098 cm^{-1}.

Other than characteristic Amide I, II and III, these spectra present some recognizable features. The peak around 1415 cm^{-1} is associated with carbonyl-containing carboxyl groups, whereas the peak at 1458 cm^{-1} is attributed to general C-H deformations [34].

A focus on the three curves Amide I bands, which were analysed as previously described through Fourier Deconvolution, is provided in Figure 18.

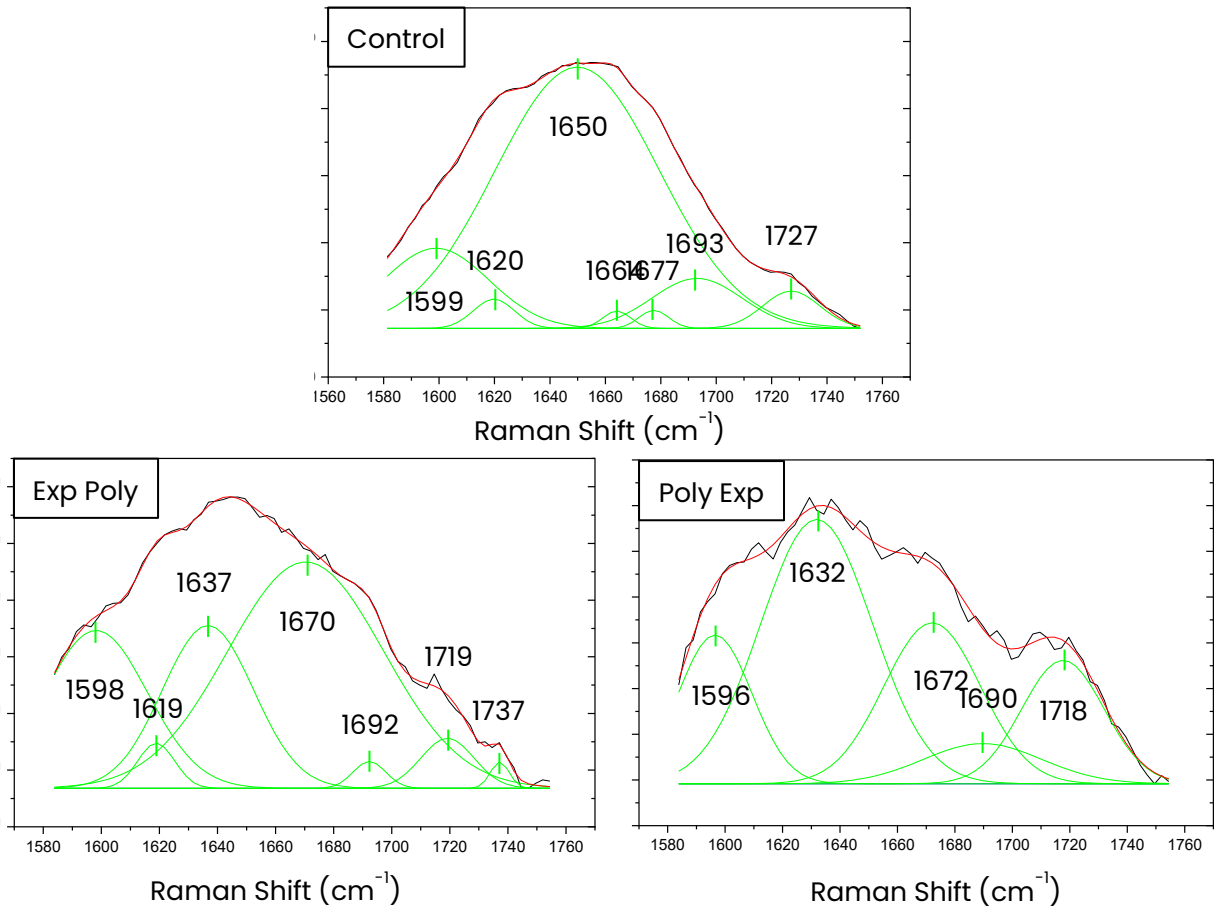

Figure 18. *Peak Deconvolution of the Amide I band of Control, Exposed Polymerised tubulin and Polymerised Exposed tubulin*

The three samples present very different Amide I band. In particular, the control showed a large peak at 1650 and many little peaks at 1599, 1620, 1664, 1677, 1693 and 1727 cm^{-1}. The Exposed Polymerised spectra still present a shoulder, sightly moved to 1619 cm^{-1}. The other features, except for the 1598 and 1692 peaks, shift a lot. In table 7 is reported each centre peak value and which secondary structure it represents.

Additional information we can derive from Figure 18 regard the lower wavenumbers range (1620-1580 cm^{-1}) of the Raman spectra, related to aromatic side chains. Indeed, the 1620-1580 cm^{-1} frequency range is typical of phenyl ring vibrational modes. In particular, the

observed peaks, present in the Exposed Polymerised and Control samples (1619-1620 cm^{-1}), can be attributed to tyrosine (Tyr) residues contributions [63].

Table 7. *Centre peak values (cm^{-1}) are highlighted to identify their respective secondary structure. β-sheets are in green, α-helixes in red, Radom coils in yellow and β-turns in blue. The corresponding bands are reported below*

Tubulin solution		
Control	Exp Poly	Poly Exp
1599	1598	1596
1620	1619	1632
1650	1637	1672
1664	1670	1690
1677	1692	1718
1693	1719	
1727	1737	

Amide I		
α-helix	1649-1660	
β-sheet	1620-1648	1665-1680
β-turn	1680-1699	
Random coil	1660-1665	

Both the Exposed samples show an increase of β-sheet and present β-turn structures (Figure 19).

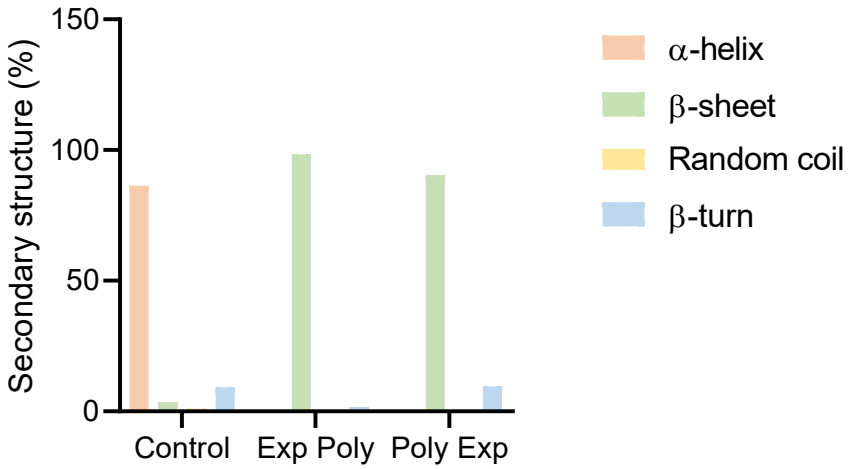

Figure 19. *Percentage of secondary structure present in each sample*

4.2.2. THz

In Figure 20 are reported the fingerprint regions (<1800cm^{-1}) of our powder tubulin samples respectively 1h and 24h after the THz exposure. The frequencies of the bands in the solid phase are different from those in the liquid phase. Some bands can shift considerably [64]. An example is indeed the Amide I band, reported in Figure 21.

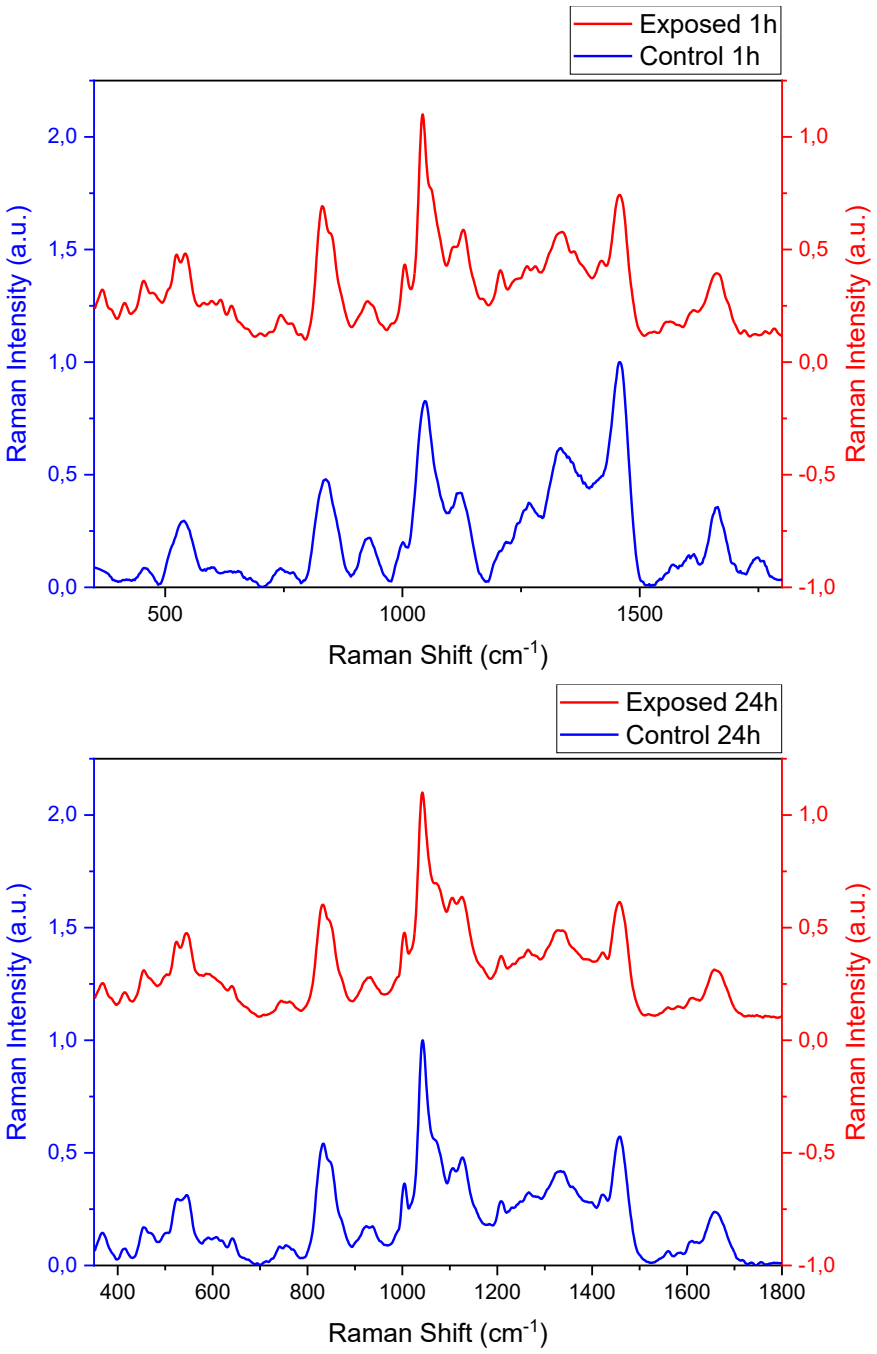

Figure 20. *Raman spectra of exposed tubulin powder samples read at two different timepoints after the exposure (1h and 24h). Control curves in blue, Exposed curves in red*

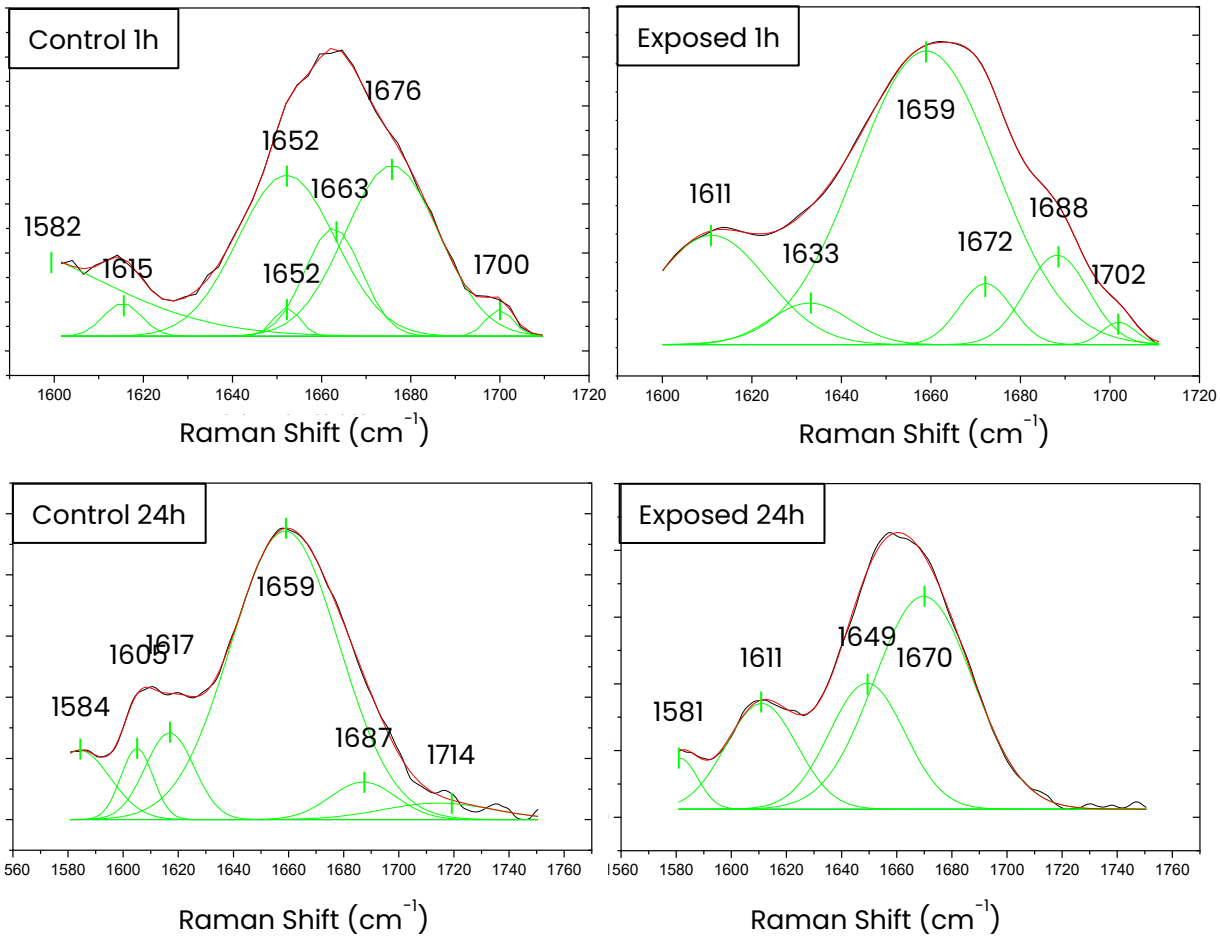

Figure 21. *Peak Deconvolution of the Amide I band of Control and Exposed samples at two different timepoints (1h and 24h) after THz exposure*

In this case, many peak differences can be detected. Starting with the 1h samples two new features at 1633 cm^{-1} and 1672 cm^{-1} appear in the Exposed curve, while the others (1615, 1652, 1663, 1676 and 1700 cm^{-1}) are slightly shifted to new values (1611, 1659, 1672, 1688 and 1702 cm^{-1}).

For the 24h samples, the features at 1584 and 1605 are moved to 1581 and 1611 cm^{-1}, while the control peak at 1617 cm^{-1} disappears in the exposed sample. Looking carefully at the spectra (Figure 21) is possible to see a little hump that was not detected during the deconvolution, probably due to its lower energy. The 1659 cm^{-1} peak moved to 1649 cm^{-1} and decrease considerably its area; on the other hand, the one at 1687 cm^{-1} shifted to 1670 cm^{-1} and increase its area.

The two control spectra show different peaks, especially in the early 1600 cm^{-1} zone.

The peak at 1605 cm^{-1} could be an indication of a medium-weak glutamate or a weak proline peak. The feature at 1615 (which shift to 1617cm^{-1} in the second control curve) belongs to tryptophan [63].

Table 8. *Centre peak values (cm^{-1}) are highlighted to identify their respective secondary structure. β-sheets are in green, α-helixes in red, Radom coils in yellow and β-turns in blue.*

SOLID			
1h		24 h	
Control	Exposed	Control	Exposed
1582	1611	1584	1581
1615	1633	1605	1611
1652	1659	1617	1649
1652	1672	1659	1670
1663	1688	1687	
1676	1702	1714	
1700			

Figure 22 reports the Deconvolution of the powder tubulin Amide III band.

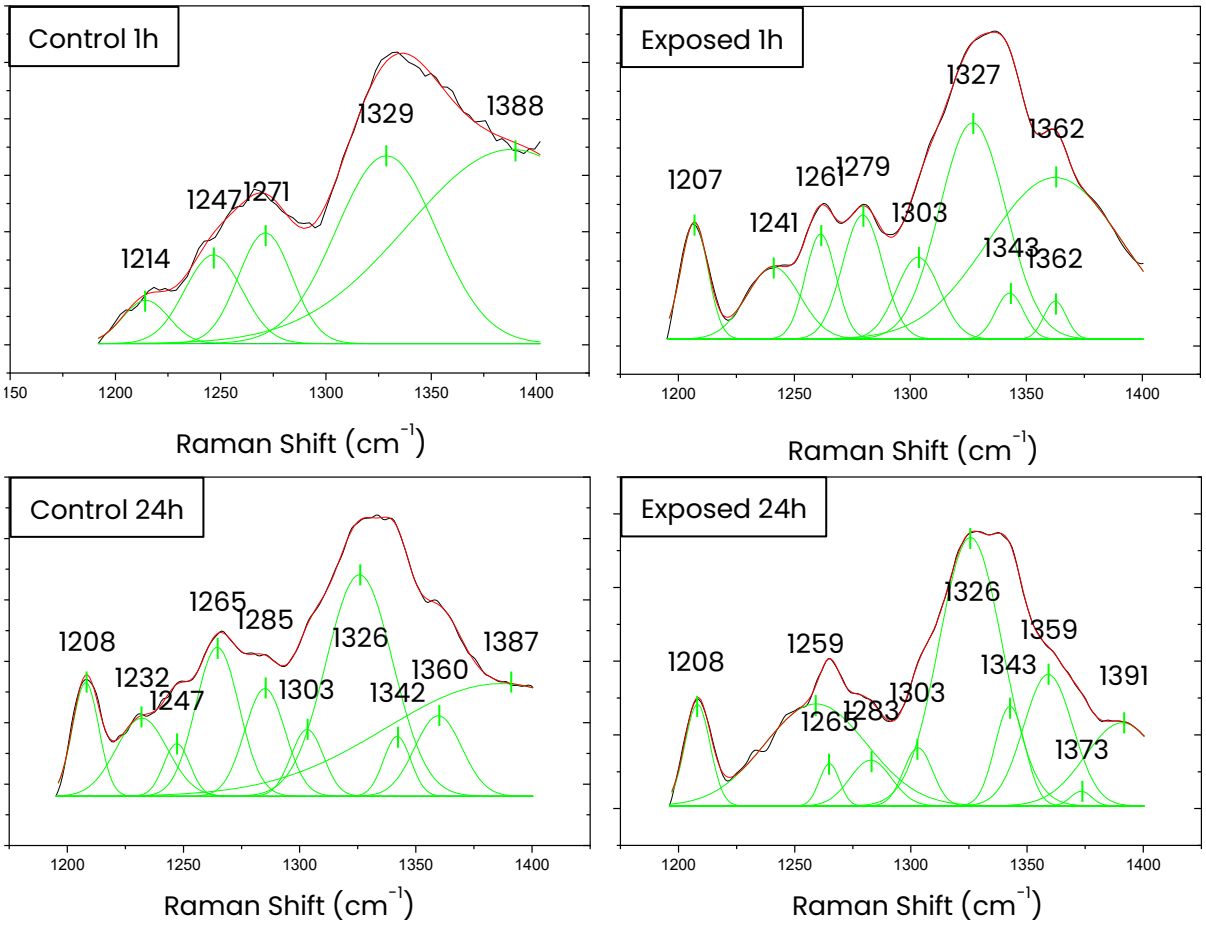

Figure 22. *Peak Deconvolution of the Amide III band of Control and Exposed samples at two different timepoints (1h and 24h) after THz exposure*

The 1207 cm^{-1} peak, belonging to the Exposed 1h curve, shifts to 1208 cm^{-1} in both the control and exposed 24h samples, while is not present in the 1h control curve. This particular feature could represent a tryptophan peak. Peaks at 1329 cm^{-1} in the 1h control sample (which shift to 1327 cm^{-1} in the exposed sample) can be attributed to moderate to strong

peaks in serine, tyrosine, or tryptophan. The same peak appears to be centred in 1326 cm^{-1} for both Control and Exposed 24h spectra. The feature at 1342 cm^{-1} in the 24h control sample could be referring to a small shoulder valine peak, which intensifies in the exposed sample (shifting to 1343 cm^{-1}). 1360 cm^{-1} (control 24h, shifted to 1359 cm^{-1} in the Exposed 24h curve) can denote a medium-weak cytosine or medium guanine peak [63]. In the Amide III range, our samples showed:

Table 9. *Centre peak values (cm^{-1}) are highlighted to identify their respective secondary structure. β-sheets are in green, α-helixes in red, Radom coils in yellow and β-turns in blue. The corresponding bands are reported below*

SOLID			
1h		24 h	
Control	Exposed	Control	Exposed
1214	1207	1208	1208
1247	1241	1232	1259
1271	1261	1247	1265
1329	1279	1265	1283
	1303	1285	1303
		1303	

Amide III	
a-helix	1260-1310
b-sheet	1235-1242
random coil	1242-1250

The area below peaks in the Amide I band is utilised to assess the relative amount of each secondary protein structure linked with different secondary structures [31], therefore we used it to calculate the percentage of each secondary structure. The values are reported in Figure 23.

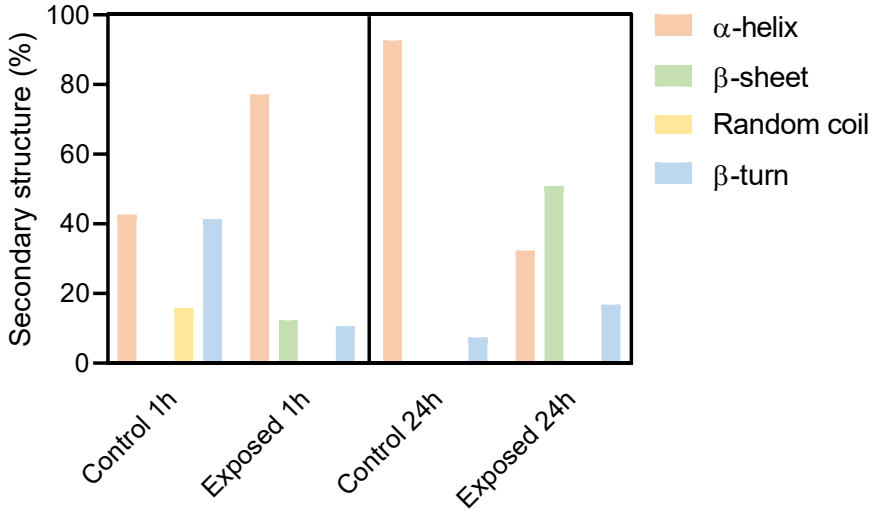

Figure 23. *Percentage of secondary structure present in each sample*

For dry samples, we have, upon exposition, an increase of α-helix and β-sheet content for the 1h samples, while a similar behaviour to the liquid samples is followed by the 24 samples (decrease of α-helices and increase in β-sheets).

4.3. Cell exposure

Non-irradiated cells, who served as the control, were cultured on the same plate since no proximity effects were detected from the first experiment.

No statistically significant difference in proliferation was found in synchronized MCF7 cells exposed for 20 minutes.

No statistically significant difference in proliferation was found in unsynchronized MCF7 cells exposed for 2 and 20 minutes with respect to each control. Similar results were found with the A2058 cell line, extending also the 1h exposed samples.

On the other hand, a decrease in proliferation was observed after 1h exposure in unsynchronized MCF7 cells as is documented in Figure 24. This inhibition was statistically significant for Day 1, Day 3, Day 4, Day 5, Day 6, and Day 7 (P values respectively: 0.0195, 0.038, 0.0037, 0.0002, 0.0062, and 0.0033).

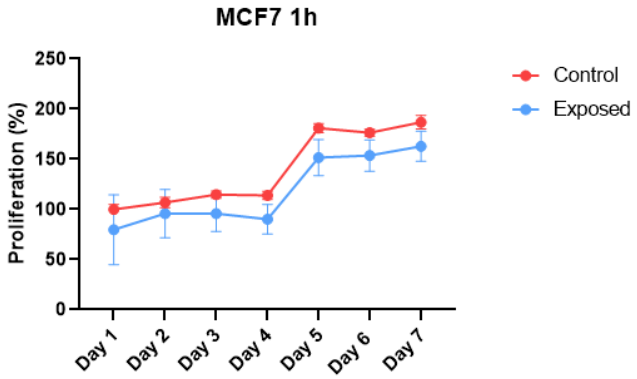

Figure 24. MCF7 1 hour stimulation: % proliferation values normalized with respect to the first day of the controls average. The two profiles are 'Control' in red and 'Exposed' in Light blue.

At the end of the treatment, cells were counted using the haemocytometer. After the 1-hour treatment, 30.91% fewer cells were found in the treated wells with respect to the controls.

We tested the hypothesis that the Vielight effect on cells could be temporary in time, therefore not detected cause of the 4-5 hours incubation time needed by the Resazurin compound to act efficiently. The incubation time is proportional to cells density; hence we cultured a 100.000 cell plate to achieve a higher cell density and cut down the waiting time to 1 hour. Even in this scenario, no substantial difference in proliferation was found.

5. Discussion

5.1. Turbidity

Tubulin behaviour appears to be different depending on the concentration of the protein exposed. Less concentrated tubulin polymerisation seems to be affected negatively by the Vielight exposure, meaning fewer MTs are formed with respect to the control curve. The curves slopes, which are an indication of the polymerisation rate of the tubulin, are also different; in this case, their ratio (control/exposed) is 1,430. The lower plateau and the smaller slope, detected in the exposed samples, are signs of a decreased amount of polymerised tubulin. Finally, the curve lag times are slightly different with a higher value for the exposed samples. This leads us to believe that the irradiation of the samples slows down to some extent the nucleation process of the MTs formation while also slowing down the growth process.

This behaviour is not seen in the more concentrated tubulin samples where, instead, the polymerisation is enhanced. For the exposed samples the plateau is reached at a higher value and the slope control/exposed ratio is 0,687, depicting a completely opposite situation as before.

One of the hypotheses that could explain this effect is based on the hormesis phenomenon. This phenomenon was first proposed by Schulz (1887, 1888) and has been well documented since then. If an environmental agent is characterized by a low dose stimulation, it appears to be beneficial to the target; on the contrary, when delivered with a high dose its effect could be inhibitory or toxic [65].

This hypothesis is based on the fact that the 2,5 mg/ml tubulin samples receive a higher dose of irradiation even though the settings on the device are not changed. In reality, the situation we are facing is a complex multi-body problem, so it might be hard to say confidently without a simulations analysis of what is happening. Indeed, multiple scattering effects occur when the light hit a target; therefore, it is difficult to assert if the samples are reached by a higher dose of light. What we can say with certainty is that more analysis is required to unravel this complexity. Future studies could involve the use of a new concentration of tubulin, in the range between the ones here analysed; or some alterations could be made to the environment to make it 'more physiological' by including ions (K^-, Cl^-) and varying the ionic concentration of the samples, increase the glycerol concentration and add MAPs.

The exposure could have interfered with the hydrogen bonds. This particular aspect was analysed through Raman Spectroscopy analysis. Hydrogen bonding is known to be important in the creation and stabilization of protein secondary structure. Secondary structures such as the α-helix and β-sheet conformations are stabilized by inter-peptide hydrogen bonding, while peptide-water hydrogen bonding competes with them, stabilizing extended conformations [66].

5.1.1. Hydration

It is important to remember that our samples are solubilized in a solution of different buffers (see Section 3.1.1); therefore, they will interact with the adjacent solute, creating what is known as a 'hydration shell' surrounding themselves.

According to terahertz spectroscopy studies, the dynamic hydration shell around proteins can extend to more than 15 Å, corresponding to at least five layers of water molecules [67]. Simultaneously, the ability of proteins to induce the structuring of their interfacial water layer has been shown to play a critical role in protein biological functions like folding, enzymatic reactions, and protein-protein interactions [67], [68].

To analyse how tubulin dimers interact with the environment, we are going to use an ideal model. Smoluchowski proposed a simple mathematical description of diffusion-controlled reactions at the molecular level. His model suggested that a reaction would occur when two reactants were sufficiently close and, more specifically, presented a brief relationship between the relative proximity of two reactants at the time of reaction and the macroscopic reaction rate.

His result can be stated using the simple example of a closed system containing two diffusing spheres with radii denoted R_1 and R_2, respectively. Diffusing hard spheres placed at random in a sufficiently large container of volume V will come into contact at a constant rate K per unit time after an initial period, following the law:

$$K = \frac{k}{V} = \frac{4\pi(D_1 + D_2)(R_1 + R_2)}{V}$$

Where D_1 and D_2 are the Einstein diffusion coefficients of spheres 1 and 2, respectively.

We can also define the effective radius σ as the sum of R_1 and R_2, which describes how close molecules must be to each other for reactions to occur at the rate specified by K [69].

In our case, we can consider tubulin dimers (sphere of radius R_t) interacting with each other inside a solution of diffusion coefficient D.

The differences in our samples concentration directly translate into distance differences between tubulin dimers. In the 5mg/ml tubulin samples, each tubulin dimer is approximately 5nm apart from one another, while this value increase in the 2,5 mg/ml samples (40% more). For two compounds to interact with each other, their distance must be, as previously stated, less than σ.

D is proportional to another parameter the frictional coefficient f.

$$D = \frac{K_B T}{f} = \frac{K_B T}{6\pi R\eta}$$

Where K_B is the Boltzman constant, T is the absolute temperature, R is the radius of the sphere and η is the solvent viscosity [67].

We suspect that D (and consequently σ) may be modified by the NIR exposure.

There is evidence that red-to-near infrared (R-NIR) photons and, presumably, other wavelengths (for which bulk water is practically transparent) interact with the bound water, i.e., interfacial water layers (IWL). The interaction has at least two biologically significant effects: increased IWL density (volume expansion) and decreased IWL viscosity [71].

These findings point to an increase in the radius of the sphere, while the D dependence is more complicated to address.

As previously mentioned, D is influenced by both R and η. While R increase upon irradiation, η decrease; therefore, D variation depends on the amount with which these parameters are varied.

Ultimately, we believed that D decreases, making it more difficult for the tubulin dimers to move within the solution.

Furthermore, it has been reported that IR exposure increases protein interfacial water H-bond cooperativeness and strength, as well as enhances structuring of the hydration shell which protects proteins against non-specific aggregation in solution, favouring periodic self-assembly [67]. Therefore, we hypothesis that a more structured hydration shell could implicate less mobility which translates into a lower value of D.

In figure 25 are depicted our two different scenarios:

2,5 mg/ml tubulin presents further tubulin dimers. In this situation, the reduction of mobility influences more MTs formation (even though the hydration radius is increased with respect to the control).

On the other hand, 5 mg/ml samples, which show closer tubulin dimers, although their mobility is still impaired, can polymerise more due to their greater radius.

This hypothesis could explain the dual turbidity behaviour we reported previously.

Tubulin concentration in living cells could be up to 24μM (2.4mg/ml) [72]; therefore, even though different concentration yields different results, based on our result, we assume that the Vielight effect in 'In Vivo' environment would impede MTs polymerisation.

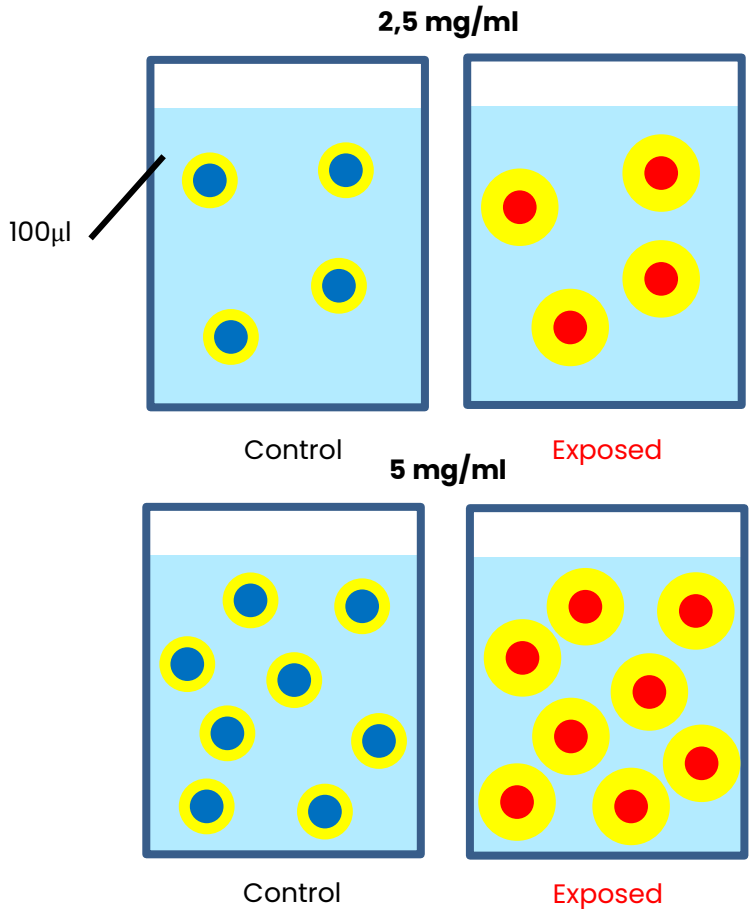

***Figure 25**. Scheme of 2,5 and 5 mg/ml tubulin samples with and without Vielight irradiation. In yellow is represented the hydration shell that expands upon exposure*

5.1.2. Exposed GTP

We decided to expose GTP to understand what component of the reaction was affected by the stimulation and, if it was affected, to what extent. Three are the main effect that Vielight could be promoting: stabilizing/destabilizing tubulin or MTs and influencing GTP.

Regarding GTP exposure, Vielight could either favour or hinder GTP hydrolyses.

The density we delivered to the sample, with a 30-minute stimulation (22,5 J/cm^2), is not enough to cause hydrolysis; therefore, a more intense stimulation is required to either rebut or validate this first scenario.

On the other hand, a way to determine if GTP hydrolysis is blocked is to look at the lag time; if it increases then this process is hampered [73].

The turbidity curves of our samples showed a slightly bigger lag time with respect to their control, but this difference was not significant. Further analyses are needed to assert if Vielight exposure actually affects GTP or it influences MTs polymerisation through other mechanisms.

5.1.3. Taxol and CCI-001

Finally, the turbidity measurements for tubulin with Taxol and CCI-001 show that Taxol behaviour is consistent with what is documented in the literature: Taxol stabilises MTs,

removing the lag time and increasing the polymerisation growth and the total amount of tubulin that polymerizes [74], [75].
On the other hand, CCI-001 at lower concentrations binds to the tubulin and prolong the nucleation phase. Longer analyses revealed that the polymerisation, in this case, is not completely inhibited, most likely due to the different tubulin CCI-001 ratios. Not enough CCI-001 is administered to completely inhibit tubulin polymerization, but just enough to delay and partially impair the process.

Something different seems to be happening with the 225μM concentration. Even though the turbidity curve shows a large standard deviation, the trend of the curve is rising with time, indicating that tubulin is polymerising. A hypothesis that could explain this behaviour is that lots of 1μm MTs are being formed. If that was the case, considering that light wavelength is 1μm, it would be possible to see a higher absorbance. To support this idea, a Mie scattering model should be created.

5.2. Raman Spectroscopy

Raman spectroscopy results appear to indicate that both THz and Vielight irradiation interact with the protein, modifying its secondary structures as evidenced by changes in the Amide I band (Figures 15, 18 and 21).

In particular, the Vielight tubulin exposed samples show, in the Amide I range, a redshift of the frequencies coupled with an intensity peaks reduction. This latter characteristic is more evident for Polymerised Exposed samples, but still present in the Exposed Polymerised spectra (Figure 17).

The frequency shift could be an indication of something changing with the hydrogen bonds of water and the C=O groups. Indeed, the shape and position of the Amide I band are determined by water's hydrogen bonding with the C=O group. When C=O···H_2O hydrogen bonds form, the length of the C=O bond increases while the C–N bond shortens, stabilising the charged structure. This is followed by a shift in the Raman Amide I band to lower wavelengths, attributed to the carbonyl group C=O's stretching vibration becoming less rigid [76].

During hydration, the N-H groups in β-sheet conformation form hydrogen bonds with the water molecules, while α-helical structures, where the N-H groups are protected by intramolecular hydrogen bonds with the carbonyl groups, do not [76]. Both tubulin and actin Vielight exposed samples are characterized by a substantial increase of the β-sheet structures at the expense of α-helix content. Upon exposition, α-helical hydrogen N-H···O=C bonds could interact with light and stretch (as testified by the redshift in frequencies). Stretched helical structures could interact with water and other unfolded structures, resulting in β-sheets formation.

The conversion of α-helix to a β-sheet in proteins is reported in the literature and was observed under the effect of multiple factors, including solvent composition alterations [77].

Since GDP- and tubulin GTP-tubulin bound states can be distinguished based on antiparallel β-sheets content [1] (even though Raman cannot distinguish the two β-sheet forms), an increase in exposed tubulin β-sheets could indicate the loss of the GTP cap and the start of the catastrophic transition of MTs.

We believe that both tubulin and MTs are affected by Vielight exposure. By looking at the intensity of the Amide I band, we presume that MTs are influenced to a wider extent.

5.2.1. THz exposure

Even though the powder samples were not GTP bound, structural changes may indicate that GTP will no longer be well bonded with the protein.

The theoretical model suggested that terahertz wave radiation cannot cause chemical covalent bond rupture or reconstruction. However, it has the potential to excite the rotational energy level of proteins, causing them to change their spatial conformation, influencing protein interactions [78]. Our results show a modification of tubulin secondary structure which may be caused by rearrangement upon molecular rotation.

Upon exposure, the two timepoints we defined, provided us with two very different spectra. In the 1h sample, it was possible to detect an increase in the amount of α-helices and β-sheet with a consequent decrease of the β-turns and random coils. The 24h samples, on the other hand, presented the same trend as the solubilised tubulin samples: an increase in β-sheet content at the expense of the α-helices. Although the behaviour of the two timepoints differs, in both cases, the intensity of the peaks seems not affected.

Two important factors that influence protein morphology, that must be considered when using the pulsed THz sources, are heat and the generation of acoustic waves in aqueous solutions [79]. THz pulses have recently been discovered to cause shockwaves at the surface of liquid water. Section 2.3.1.2 gives an example of this type of behaviour. THz-induced shockwaves may cause mechanical stress in biomolecules, altering their shape. These indirect effects of THz irradiation have not been studied thoughtfully [28].

Our samples are in the solid state; therefore, the latter effect is not present. Temperature, on the other hand, induces denaturation which is characterized by the loss of all regular repeating patterns (α-helices and β-sheets) and the adoption of a random coil structure [80]. These changes were not detected in our samples; hence we will refute temperature-induced modifications.

The detected difference in secondary structure was also present between the two controls. This suggests that a dependence on time is present and that external parameters are influencing the 24h samples, however, they might be affecting both control and exposed sample the same way. However, further analyses are needed.

5.3. Proliferation

Finally, we are going to discuss how Vielight affected cancer cells proliferation. In their work, Hamblin et al. asked if it was better to directly irradiate the tumour or to direct the light to the bone marrow, lymphatic organs, or even the entire body if the goal was to stimulate the immune system [55]. We discovery that low doses stimulations do not help or harm in any way cancer cells proliferation; hence, the former is not a suitable option.

Although, if the dose increases significantly, the treatment did limit cells proliferation in the case of the MCF7 cell line.

In their study, Cialdai et al. found that, in comparison to the untreated controls, the vitality and proliferation rate of fibroblasts, MCF-7, and MDA-MB361 cancer cells exposed to laser treatment did not differ substantially. Their treatment consisted of 10 min, with 1500 Hz frequency, duty cycle 50%, energy density 9 J/cm^2, irradiance 15 mW/cm^2. It was repeated once a day, for three consecutive days, similar to our set-up [52]. Their findings support our MCF7 results for low dose irradiations. Another research reported that high irradiance was highly effective compared to low irradiance in terms of inhibition [81]. Therefore, the answer depends on the parameters used and the cell line that is going to be exposed.

6. Bibliography

[1] R. Audenaert, L. Heremans, K. Heremans, and Y. Engelborghs, “Secondary structure analysis of tubulin and microtubules with Rarnan spectroscopy *,” 1989.

[2] C. Janke and M. M. Magiera, “The tubulin code and its role in controlling microtubule properties and functions,” *Nature Reviews Molecular Cell Biology*, vol. 21, no. 6. Nature Research, pp. 307–326, Jun. 01, 2020. doi: 10.1038/s41580-020-0214-3.

[3] C. F. Beyer *et al.*, “TTI-237: A novel microtubule-active compound with in vivo antitumor activity,” *Cancer Research*, vol. 68, no. 7, pp. 2292–2300, Apr. 2008, doi: 10.1158/0008-5472.CAN-07-1420.

[4] M. A. H. Albahde *et al.*, “The Role of Microtubules in Pancreatic Cancer: Therapeutic Progress,” *Frontiers in Oncology*, vol. 11. Frontiers Media S.A., May 21, 2021. doi: 10.3389/fonc.2021.640863.

[5] S. Roychowdhury and J. A. Sierra-Fonseca, “Heterotrimeric G Proteins and the Regulation of Microtubule Assembly,” in *Cytoskeleton - Structure, Dynamics, Function and Disease*, InTech, 2017. doi: 10.5772/66929.

[6] G. Li and J. K. Moore, “Microtubule dynamics at low temperature: Evidence that tubulin recycling limits assembly,” *Molecular Biology of the Cell*, vol. 31, no. 11, pp. 1154–1166, May 2020, doi: 10.1091/MBC.E19-11-0634.

[7] E. Pasquier and M. Kavallaris, “Microtubules: A dynamic target in cancer therapy,” *IUBMB Life*, vol. 60, no. 3. pp. 165–170, 2008. doi: 10.1002/iub.25.

[8] F. Borys, E. Joachimiak, H. Krawczyk, and H. Fabczak, “Intrinsic and Extrinsic Factors Affecting Microtubule Dynamics in Normal and Cancer Cells,” *Molecules*, vol. 25, no. 16. MDPI AG, Aug. 01, 2020. doi: 10.3390/molecules25163705.

[9] S. Honore, E. Pasquier, and D. Braguer, “Understanding microtubule dynamics for improved cancer therapy,” *Cellular and Molecular Life Sciences*, vol. 62, no. 24. pp. 3039–3056, Dec. 2005. doi: 10.1007/s00018-005-5330-x.

[10] V. Čermák *et al.*, “Microtubule-targeting agents and their impact on cancer treatment,” *European Journal of Cell Biology*, vol. 99, no. 4. Elsevier GmbH, May 01, 2020. doi: 10.1016/j.ejcb.2020.151075.

[11] Y. Lu, J. Chen, M. Xiao, W. Li, and D. D. Miller, “An overview of tubulin inhibitors that interact with the colchicine binding site,” *Pharmaceutical Research*, vol. 29, no. 11. pp. 2943–2971, Nov. 2012. doi: 10.1007/s11095-012-0828-z.

[12] E. C. McLoughlin and N. M. O’boyle, “Colchicine-binding site inhibitors from chemistry to clinic: A review,” *Pharmaceuticals*, vol. 13, no. 1. MDPI AG, Jan. 01, 2020. doi: 10.3390/ph13010008.

[13] E. H. Kellogg *et al.*, “Insights into the Distinct Mechanisms of Action of Taxane and Non-Taxane Microtubule Stabilizers from Cryo-EM Structures,” *Journal of Molecular Biology*, vol. 429, no. 5, pp. 633–646, Mar. 2017, doi: 10.1016/j.jmb.2017.01.001.

[14] M. O. Steinmetz and A. E. Prota, “Microtubule-Targeting Agents: Strategies To Hijack the Cytoskeleton,” *Trends in Cell Biology*, vol. 28, no. 10. Elsevier Ltd, pp. 776–792, Oct. 01, 2018. doi: 10.1016/j.tcb.2018.05.001.

[15] Lifeng He, George A. Orr, and Susan Band Horwitz, “Novel molecules that interact with MTs and have functional activity similar to Taxol,” *Drug Discovery Today*, vol. 6, 2001, doi: 10.1016/s1359-6446(01)02038-4.

[16] National Center for Biotechnology Information, “PubChem Compound Summary for CID 4666, Taxol,” *PubChem*. https://pubchem.ncbi.nlm.nih.gov/compound/Taxol (accessed Dec. 02, 2021).

[17] A. Spada *et al.*, “Albumin Nanoparticles for the Delivery of a Novel Inhibitor of β-tubulin Polymerization,” 2021. [Online]. Available: www.cspsCanada.org
[18] C. M. Hough *et al.*, “Disassembly of microtubules by intense terahertz pulses,” *Biomedical Optics Express*, vol. 12, no. 9, p. 5812, Sep. 2021, doi: 10.1364/boe.433240.
[19] Cameron M. Hough *et al.*, “Biological Effects of Intense THz Pulses on Human Skin Tissue Models”.
[20] O. P. Cherkasova, V. I. Fedorov, E. F. Nemova, and A. S. Pogodin, “Influence of terahertz laser radiation on the spectral characteristics and functional properties of albumin,” in *Optics and Spectroscopy (English translation of Optika i Spektroskopiya)*, 2009, vol. 107, no. 4, pp. 534–537. doi: 10.1134/S0030400X09100063.
[21] V. M. Govorun *et al.*, “Far-Infrared radiation effect on the structure and properties of proteins,” 1991.
[22] I. v. Lundholm *et al.*, “Terahertz radiation induces non-thermal structural changes associated with Fröhlich condensation in a protein crystal,” *Structural Dynamics*, vol. 2, no. 5, Sep. 2015, doi: 10.1063/1.4931825.
[23] L. Sun, L. Zhao, and R. Y. Peng, “Research progress in the effects of terahertz waves on biomacromolecules,” *Military Medical Research*, vol. 8, no. 1. BioMed Central Ltd, Dec. 01, 2021. doi: 10.1186/s40779-021-00321-8.
[24] Shota Yamazaki *et al.*, *Terahertz irradiation stimulates actin polymerization*. IEEE, 2018.
[25] H. Hoshina, S. Yamazaki, M. Tsubouchi, and M. Harata, “Terahertz irradiation effects on the morphology and dynamics of actin biopolymer,” *JPhys Photonics*, vol. 3, no. 3, Jul. 2021, doi: 10.1088/2515-7647/ac0958.
[26] R. Dominguez and K. C. Holmes, “Actin structure and function,” *Annual Review of Biophysics*, vol. 40, no. 1, pp. 169–186, Jun. 2011, doi: 10.1146/annurev-biophys-042910-155359.
[27] Chris T. Zimmerle and Carl Frieden, “Effect of Temperature on the Mechanism of Actin Polymerization,” 1986.
[28] S. Yamazaki *et al.*, “Propagation of THz irradiation energy through aqueous layers: Demolition of actin filaments in living cells,” *Scientific Reports*, vol. 10, no. 1, Dec. 2020, doi: 10.1038/s41598-020-65955-5.
[29] T. Miura and G. J. Thomas, “Raman Spectroscopy of Proteins and Their Assemblies.”
[30] C. H. Camp *et al.*, “High-speed coherent Raman fingerprint imaging of biological tissues,” *Nature Photonics*, vol. 8, no. 8, pp. 627–634, 2014, doi: 10.1038/nphoton.2014.145.
[31] A. Sadat and I. J. Joye, “Peak fitting applied to fourier transform infrared and raman spectroscopic analysis of proteins,” *Applied Sciences (Switzerland)*, vol. 10, no. 17, Sep. 2020, doi: 10.3390/app10175918.
[32] N. Kuhar, S. Sil, and S. Umapathy, “Potential of Raman spectroscopic techniques to study proteins,” *Spectrochimica Acta - Part A: Molecular and Biomolecular Spectroscopy*, vol. 258. Elsevier B.V., Sep. 05, 2021. doi: 10.1016/j.saa.2021.119712.
[33] R. Gautam, S. Vanga, A. Madan, N. Gayathri, U. Nongthomba, and S. Umapathy, “Raman spectroscopic studies on screening of myopathies,” *Analytical Chemistry*, vol. 87, no. 4, pp. 2187–2194, Feb. 2015, doi: 10.1021/ac503647x.
[34] A. Rygula, K. Majzner, K. M. Marzec, A. Kaczor, M. Pilarczyk, and M. Baranska, “Raman spectroscopy of proteins: A review,” *Journal of Raman Spectroscopy*, vol. 44, no. 8. pp. 1061–1076, Aug. 2013. doi: 10.1002/jrs.4335.

[35] W. R. W. Welch, J. Kubelka, and T. A. Keiderling, “Infrared, vibrational circular dichroism, and raman spectral simulations for β-sheet structures with various isotopic labels, interstrand, and stacking arrangements using density functional theory,” *Journal of Physical Chemistry B*, vol. 117, no. 36, pp. 10343–10358, Sep. 2013, doi: 10.1021/jp4056126.

[36] N. C. Maiti, M. M. Apetri, M. G. Zagorski, P. R. Carey, and V. E. Anderson, “Raman Spectroscopic Characterization of Secondary Structure in Natively Unfolded Proteins: α-Synuclein,” *Journal of the American Chemical Society*, vol. 126, no. 8, pp. 2399–2408, Mar. 2004, doi: 10.1021/ja0356176.

[37] D. Kurouski, R. P. van Duyne, and I. K. Lednev, “Exploring the structure and formation mechanism of amyloid fibrils by Raman spectroscopy: A review,” *Analyst*, vol. 140, no. 15. Royal Society of Chemistry, pp. 4967–4980, Feb. 05, 2015. doi: 10.1039/c5an00342c.

[38] S. Bhattacharya, S. Ghosh, N. K. Pandey, S. Chaudhury, S. Dasgupta, and A. Roy, “Distribution of protein ramachandran psi (ψ) angle using non-resonance visible raman scattering measurements,” *Journal of Physical Chemistry B*, vol. 117, no. 45, pp. 13993–14000, Nov. 2013, doi: 10.1021/jp408009y.

[39] H. Ishizaki, P. Balaram, R. Nagaraj, Y. v Venkatachalapathi, and A. T. Tu, “DETERMINATION OF $-TURN CONFORMATION BY LASER RAMAN SPECTROSCOPY.”

[40] Y. Hong Ong, M. Lim, and Q. Liu, “Comparison of principal component analysis and biochemical component analysis in Raman spectroscopy for the discrimination of apoptosis and necrosis in K562 leukemia cells,” 2012.

[41] C. M. O’Brien *et al.*, “In vivo Raman spectroscopy for biochemical monitoring of the human cervix throughout pregnancy,” *American Journal of Obstetrics and Gynecology*, vol. 218, no. 5, pp. 528.e1-528.e18, May 2018, doi: 10.1016/j.ajog.2018.01.030.

[42] R. Gautam, S. Vanga, A. Madan, N. Gayathri, U. Nongthomba, and S. Umapathy, “Raman spectroscopic studies on screening of myopathies,” *Analytical Chemistry*, vol. 87, no. 4, pp. 2187–2194, Feb. 2015, doi: 10.1021/ac503647x.

[43] L. Silveira, F. L. Silveira, B. Bodanese, R. A. Zângaro, and M. T. T. Pacheco, “ Discriminating model for diagnosis of basal cell carcinoma and melanoma in vitro based on the Raman spectra of selected biochemicals ,” *Journal of Biomedical Optics*, vol. 17, no. 7, p. 077003, Jul. 2012, doi: 10.1117/1.jbo.17.7.077003.

[44] A. Y. F. You *et al.*, “Raman spectroscopy imaging reveals interplay between atherosclerosis and medial calcification in the human aorta,” *SCIENCE ADVANCES*, 2017.

[45] D. Choudhury *et al.*, “Unprecedented inhibition of tubulin polymerization directed by gold nanoparticles inducing cell cycle arrest and apoptosis,” *Nanoscale*, vol. 5, no. 10, pp. 4476–4489, May 2013, doi: 10.1039/c3nr33891f.

[46] G. Vedantham, H. G. Sparks, S. U. Sane, S. Tzannis, and T. M. Przybycien, “A Holistic Approach for Protein Secondary Structure Estimation from Infrared Spectra in H2O Solutions,” *Analytical Biochemistry*, vol. 285, no. 1, pp. 33–49, Oct. 2000, doi: 10.1006/ABIO.2000.4744.

[47] S. Hahn, S. S. Kim, C. Lee, and M. Cho, “Characteristic two-dimensional IR spectroscopic features of antiparallel and parallel β -sheet polypeptides: Simulation studies,” *Journal of Chemical Physics*, vol. 123, no. 8, Aug. 2005, doi: 10.1063/1.1997151.

[48] R. Zein, W. Selting, and M. R. Hamblin, “Review of light parameters and photobiomodulation efficacy: dive into complexity,” *Journal of Biomedical Optics*, vol. 23, no. 12, p. 1, Dec. 2018, doi: 10.1117/1.jbo.23.12.120901.

[49] A. del Vecchio *et al.*, “Laser photobiomodulation (Pbm)—a possible new frontier for the treatment of oral cancer: A review of in vitro and in vivo studies,” *Healthcare (Switzerland)*, vol. 9, no. 2. MDPI AG, Feb. 01, 2021. doi: 10.3390/healthcare9020134.

[50] S. Y. Tam, V. C. W. Tam, S. Ramkumar, M. L. Khaw, H. K. W. Law, and S. W. Y. Lee, “Review on the Cellular Mechanisms of Low-Level Laser Therapy Use in Oncology,” *Frontiers in Oncology*, vol. 10. Frontiers Media S.A., Jul. 24, 2020. doi: 10.3389/fonc.2020.01255.

[51] R. J. Bensadoun, R. G. Nair, and J. Robijns, “Photobiomodulation for Side Effects of Cancer Therapy,” *Photobiomodulation, Photomedicine, and Laser Surgery*, vol. 38, no. 6. Mary Ann Liebert Inc., pp. 323–325, Jun. 01, 2020. doi: 10.1089/photob.2019.4759.

[52] F. Cialdai *et al.*, “In vitro study on the safety of near infrared laser therapy in its potential application as postmastectomy lymphedema treatment,” *Journal of Photochemistry and Photobiology B: Biology*, vol. 151, pp. 285–296, Oct. 2015, doi: 10.1016/j.jphotobiol.2015.08.003.

[53] Y. Y. Huang, A. C. H. Chen, J. D. Carroll, and M. R. Hamblin, “Biphasic dose response in low level lightherapy,” *Dose-Response*, vol. 7, no. 4, pp. 358–383, 2009, doi: 10.2203/dose-response.09-027.Hamblin.

[54] L. F. de Freitas and M. R. Hamblin, “Proposed Mechanisms of Photobiomodulation or Low-Level Light Therapy,” *IEEE Journal of Selected Topics in Quantum Electronics*, vol. 22, no. 3, pp. 348–364, May 2016, doi: 10.1109/JSTQE.2016.2561201.

[55] M. R. Hamblin, S. T. Nelson, and J. R. Strahan, “Photobiomodulation and Cancer: What Is the Truth?,” *Photomedicine and laser surgery*, vol. 36, no. 5. pp. 241–245, May 01, 2018. doi: 10.1089/pho.2017.4401.

[56] “Low-Level Light Therapy Photobiomodulation”.

[57] J. Chiche, M. C. Brahimi-Horn, and J. Pouysségur, “Tumour hypoxia induces a metabolic shift causing acidosis: A common feature in cancer,” *Journal of Cellular and Molecular Medicine*, vol. 14, no. 4, pp. 771–794, Apr. 2010, doi: 10.1111/j.1582-4934.2009.00994.x.

[58] R. Shiratori *et al.*, “Glycolytic suppression dramatically changes the intracellular metabolic profile of multiple cancer cell lines in a mitochondrial metabolism-dependent manner,” *Scientific Reports*, vol. 9, no. 1, Dec. 2019, doi: 10.1038/s41598-019-55296-3.

[59] A. M. Otto, “Warburg effect(s)—a biographical sketch of Otto Warburg and his impacts on tumor metabolism,” *Cancer & Metabolism*, vol. 4, no. 1, Dec. 2016, doi: 10.1186/s40170-016-0145-9.

[60] M. Mirigian, K. Mukherjee, S. L. Bane, and D. L. Sackett, “Measurement of In vitro microtubule polymerization by turbidity and fluorescence,” in *Methods in Cell Biology*, vol. 115, Academic Press Inc., 2013, pp. 215–229. doi: 10.1016/B978-0-12-407757-7.00014-1.

[61] C. Bonfils, N. Bec, B. Lacroix, M. C. Harricane, and C. Larroque, “Kinetic analysis of tubulin assembly in the presence of the microtubule-associated protein TOGp,” *Journal of Biological Chemistry*, vol. 282, no. 8, pp. 5570–5581, Feb. 2007, doi: 10.1074/jbc.M605641200.

[62] J. O’brien, I. Wilson, T. Orton, and F. Ë. Ois Pognan, “Investigation of the Alamar Blue (resazurin) fluorescent dye for the assessment of mammalian cell cytotoxicity,” 2000.

[63] J. de Gelder, K. de Gussem, P. Vandenabeele, and L. Moens, “Reference database of Raman spectra of biological molecules,” *Journal of Raman Spectroscopy*, vol. 38, no. 9, pp. 1133–1147, Sep. 2007, doi: 10.1002/jrs.1734.

[64] G. Zhu, X. Zhu, Q. Fan, and X. Wan, “Raman spectra of amino acids and their aqueous solutions,” *Spectrochimica Acta - Part A: Molecular and Biomolecular Spectroscopy*, vol. 78, no. 3, pp. 1187–1195, Mar. 2011, doi: 10.1016/j.saa.2010.12.079.

[65] Carla D. Garzon and Francisco J. Flores, “Hormesis: Biphasic Dose-Responses to Fungicides in Plant Pathogens and Their Potential Threat to Agriculture,” in *Fungicides - Showcases of Integrated Plant Disease Management from Around the World*, InTech, 2013. doi: 10.5772/55359.

[66] N. S. Myshakina, Z. Ahmed, and S. A. Asher, “Dependence of amide vibrations on hydrogen bonding,” *Journal of Physical Chemistry B*, vol. 112, no. 38, pp. 11873–11877, Sep. 2008, doi: 10.1021/jp8057355.

[67] M. Kowacz and P. Warszyński, “Effect of infrared light on protein behavior in contact with solid surfaces.”

[68] Y. Tokunaga *et al.*, “Nonthermal excitation effects mediated by sub-terahertz radiation on hydrogen exchange in ubiquitin,” *Biophysical Journal*, vol. 120, no. 12, pp. 2386–2393, Jun. 2021, doi: 10.1016/j.bpj.2021.04.013.

[69] M. B. Flegg, “Smoluchowski reaction kinetics for reactions of any order,” Nov. 2015, [Online]. Available: http://arxiv.org/abs/1511.04786

[70] S. Miyamoto and K. Shimono, “Molecular Modeling to Estimate the Diffusion Coefficients of Drugs and Other Small Molecules,” *Molecules (Basel, Switzerland)*, vol. 25, no. 22, Nov. 2020, doi: 10.3390/molecules25225340.

[71] A. P. Sommer, “Mitochondrial cytochrome c oxidase is not the primary acceptor for near infrared light—it is mitochondrial bound water: the principles of low-level light therapy,” *Annals of Translational Medicine*, vol. 7, no. S1, pp. S13–S13, Mar. 2019, doi: 10.21037/atm.2019.01.43.

[72] J. Mozziconacci, L. Sandblad, M. Wachsmuth, D. Brunner, and E. Karsenti, “Tubulin dimers oligomerize before their incorporation into microtubules,” *PLoS ONE*, vol. 3, no. 11, Nov. 2008, doi: 10.1371/journal.pone.0003821.

[73] J. Roostalu and T. Surrey, “Microtubule nucleation: Beyond the template,” *Nature Reviews Molecular Cell Biology*, vol. 18, no. 11. Nature Publishing Group, pp. 702–710, 2017. doi: 10.1038/nrm.2017.75.

[74] N. Kumar, “Taxol-induced polymerization of purified tubulin. Mechanism of action,” *Journal of Biological Chemistry*, vol. 256, no. 20, pp. 10435–10441, 1981, doi: 10.1016/s0021-9258(19)68639-4.

[75] Inc. Cytoskeleton, “Tubulin Polymerization Assay Kit.” https://www.cytoskeleton.com/pdf-storage/datasheets/bk006p.pdf (accessed Nov. 10, 2021).

[76] C. Mensch, P. Bultinck, and C. Johannessen, “The effect of protein backbone hydration on the amide vibrations in Raman and Raman optical activity spectra.”

[77] Z. Qin and M. J. Buehler, “Molecular dynamics simulation of the α-helix to β-sheet transition in coiled protein filaments: Evidence for a critical filament length scale,” *Physical Review Letters*, vol. 104, no. 19, May 2010, doi: 10.1103/PhysRevLett.104.198304.

[78] L. Sun, L. Zhao, and R. Y. Peng, “Research progress in the effects of terahertz waves on biomacromolecules,” *Military Medical Research*, vol. 8, no. 1. BioMed Central Ltd, Dec. 01, 2021. doi: 10.1186/s40779-021-00321-8.

[79] S. Yamazaki *et al.*, “THz irradiation inhibits cell division by affecting actin dynamics,” *PLoS ONE*, vol. 16, no. 8 August, Aug. 2021, doi: 10.1371/journal.pone.0248381.

[80] S. R. Sivaramakrishnan, “Microwave Pasteurization of Shell Eggs-A Comprehensive Study,” 2010.

[81] Z. Chen, W. Li, X. Hu, and M. Liu, “Irradiance plays a significant role in photobiomodulation of B16F10 melanoma cells by increasing reactive oxygen species and inhibiting mitochondrial function,” *Biomedical Optics Express*, vol. 11, no. 1, p. 27, Jan. 2020, doi: 10.1364/boe.11.000027.

7. Supporting information

Sigmoidal fit related information

7.1. 2,5 mg/ml tubulin

Model	**Boltzmann**
Equation	y = A2 + (A1-A2)/(1 + exp((x-x0)/dx))
Plot	Control
A1	-0,00341 ± 2,46548E-4
A2	0,08734 ± 3,63593E-4
x0	1366,55245 ± 3,70688
dx	272,93708 ± 3,63691
Reduced Chi-Sqr	7,46367E-7
R-Square (COD)	0,99937
Adj. R-Square	0,99934

Model	**Boltzmann**
Equation	y = A2 + (A1-A2)/(1 + exp((x-x0)/dx))
Plot	Exposed
A1	-0,00181 ± 2,27712E-4
A2	0,07407 ± 5,65072E-4
x0	1559,63073 ± 6,04738
dx	298,98567 ± 5,33246
Reduced Chi-Sqr	7,13484E-7
R-Square (COD)	0,99897
Adj. R-Square	0,99893

7.2. Exposed GTP

Model	**Boltzmann**
Equation	y = A2 + (A1-A2)/(1 + exp((x-x0)/dx))
Plot	Control
A1	-0,00328 ± 2,1572E-4
A2	0,09058 ± 2,49335E-4
x0	1264,78368 ± 2,71241

dx	258,9442 ± 2,67565
Reduced Chi-Sqr	5,26153E-7
R-Square (COD)	0,99961
Adj. R-Square	0,99959

Model	**Boltzmann**
Equation	y = A2 + (A1-A2)/(1 + exp((x-x0)/dx))
Plot	Exposed
A1	-0,00216 ± 2,69965E-4
A2	0,10699 ± 3,46504E-4
x0	1322,98763 ± 3,03266
dx	224,72316 ± 2,85289
Reduced Chi-Sqr	1,19259E-6
R-Square (COD)	0,99939
Adj. R-Square	0,99937

7.3. 2,5 mg/ml tubulin -2h exposure

Model	**Boltzmann**
Equation	y = A2 + (A1-A2)/(1 + exp((x-x0)/dx))
Plot	Control
A1	-0,00135 ± 2,01509E-4
A2	0,05723 ± 5,25929E-4
x0	1567,09462 ± 7,42549
dx	327,35858 ± 6,51466
Reduced Chi-Sqr	4,51205E-7
R-Square (COD)	0,99882
Adj. R-Square	0,99877

Model	**Boltzmann**
Equation	y = A2 + (A1-A2)/(1 + exp((x-x0)/dx))
Plot	Exposed
A1	-0,0043 ± 2,50988E-4

A2	0,06053 ± 3,14984E-4
x0	1295,1455 ± 4,80627
dx	287,60134 ± 4,89976
Reduced Chi-Sqr	5,96245E-7
R-Square (COD)	0,99899
Adj. R-Square	0,99895

7.4. 5 mg/ml tubulin

Model	**Boltzmann**
Equation	y = A2 + (A1-A2)/(1 + exp((x-x0)/dx))
Plot	Control
A1	-0,00302 ± 8,55303E-4
A2	0,13965 ± 4,02463E-4
x0	698,59913 ± 3,53354
dx	121,63755 ± 3,044
Reduced Chi-Sqr	6,75052E-6
R-Square (COD)	0,998
Adj. R-Square	0,99793

Model	**Boltzmann**
Equation	y = A2 + (A1-A2)/(1 + exp((x-x0)/dx))
Plot	Exposed
A1	-0,00154 ± 9,11779E-4
A2	0,18124 ± 3,93725E-4
x0	571,59113 ± 2,28394
dx	82,51756 ± 1,96318
Reduced Chi-Sqr	7,91199E-6
R-Square (COD)	0,99849
Adj. R-Square	0,99843

7.5. Raman Spectroscopy peak parameters

Actin

Control					
Peak Type	**Area Intg**	**Area IntgP**	**Center Grvty**	**Max Height**	**FWHM**
Gaussian	60,18311	79,68251	1632,7285	0,67661	92,50841
Gaussian	15,34552	20,31749	1671,19021	0,29653	48,62004

Exposed					
Peak Type	**Area Intg**	**Area IntgP**	**Center Grvty**	**Max Height**	**FWHM**
Gaussian	17,39483	22,21672	1595,96382	0,32359	74,38607
Gaussian	57,33722	73,23124	1655,35756	0,751	72,38335
Gaussian	3,56407	4,55204	1713,39721	0,10086	33,38011

Tubulin solution

Control					
Peak Type	**Area Intg**	**Area IntgP**	**Center Grvty**	**Max Height**	**FWHM**
Gaussian	-26,50654	-31,9713	1613,32549	0,47672	57,77992
Gaussian	-55,10259	-66,4629	1662,86332	0,76128	68,23679
Gaussian	-1,29816	-1,5658	1722,24369	0,05265	23,19211

Exposed Polymerised					
Peak Type	**Area Intg**	**Area IntgP**	**Center Grvty**	**Max Height**	**FWHM**
Gaussian	-2,51624	-4,81381	1591,2659	0,1135	28,53225
Gaussian	-0,52091	-0,99654	1618,334	0,0421	11,62335
Gaussian	-42,82867	-81,93556	1645,10545	0,5103	82,16743
Gaussian	-3,74151	-7,15789	1691,08015	0,12272	28,64065
Gaussian	-2,22618	-4,25891	1719,16697	0,10455	20,00411
Gaussian	-0,43766	-0,83729	1736,94134	0,05029	8,1754

Polymerised Exposed					
Peak Type	**Area Intg**	**Area IntgP**	**Center Grvty**	**Max Height**	**FWHM**
Gaussian	-5,84225	-17,75761	1598,7043	0,19233	33,50809
Gaussian	-9,19007	-27,9334	1631,18408	0,22493	38,45591
Gaussian	-0,47864	-1,45484	1670,54368	0,0275	16,35002
Gaussian	-13,39831	-40,7244	1670,55239	0,21019	59,93374
Gaussian	-3,99068	-12,12974	1719,42418	0,11958	31,49336

Powder tubulin

Control 1h					
Peak Type	**Area Intg**	**Area IntgP**	**Center Grvty**	**Max Height**	**FWHM**
Gaussian	1,72545	13,12235	1608,79853	0,07907	28,20839
Gaussian	10,49381	79,80713	1661,78158	0,29017	33,99068
Gaussian	0,70268	5,344	1683,5008	0,04291	15,38391
Gaussian	0,22702	1,72651	1699,62684	0,02853	7,48462

Exposed 1h					
Peak Type	**Area Intg**	**Area IntgP**	**Center Grvty**	**Max Height**	**FWHM**
Gaussian	2,41806	15,38574	1610,995	0,09629	29,06922
Gaussian	0,81719	5,19964	1632,92	0,0366	20,97711
Gaussian	10,10633	64,30496	1658,94	0,25856	36,73846
Gaussian	0,80155	5,10012	1672,23	0,05385	13,98363
Gaussian	1,38893	8,83756	1688,2	0,07881	16,56699
Gaussian	0,18419	1,17199	1701,985	0,01966	8,87845

Control 24h					
Peak Type	**Area Intg**	**Area IntgP**	**Center Grvty**	**Max Height**	**FWHM**
Gaussian	0,97826	5,89696	1584,1064	0,05659	26,35032
Gaussian	0,85045	5,12654	1604,99469	0,05811	13,74862
Gaussian	1,57667	9,50425	1616,8567	0,0708	20,92085
Gaussian	11,60823	69,97483	1658,75606	0,23583	46,24273
Gaussian	0,92113	5,55258	1687,10089	0,03073	28,16077
Gaussian	0,65441	3,94483	1714,29944	0,01349	47,2412

Exposed 24h					
Peak Type	**Area Intg**	**Area IntgP**	**Center Grvty**	**Max Height**	**FWHM**
Gaussian	0,33157	2,49618	1581,43504	0,03799	15,19995
Gaussian	2,5351	19,08532	1610,93715	0,07914	30,3895
Gaussian	3,25016	24,46857	1649,26159	0,09434	32,36397
Gaussian	7,16617	53,94994	1669,75326	0,1595	42,20867

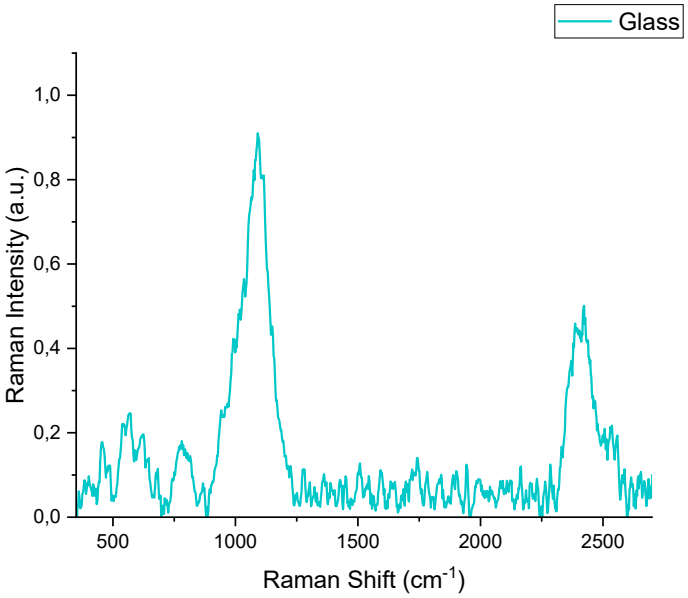

Glass Raman spectra